This manuscript represents a pre-print of a manuscript that has undergone peer-review and has been accepted for publication with Geochimica et Cosmochimica Acta.

Constraints on the behaviour and content of volatiles in Galápagos magmas from melt inclusions and nominally anhydrous minerals

Matthew L. M. Gleeson[1,2]*, Sally A. Gibson[2], Michael J. Stock[3], and EIMF[4]

[1]School of Earth and Environmental Sciences, Cardiff University, Main Building, Park Place, Cardiff, CF10 3AT, UK.

[2]Department of Earth Sciences, University of Cambridge, Downing Street, Cambridge, CB2 3EQ, UK.

[3]Department of Geology, Trinity College Dublin, College Green, Dublin 2, Ireland.

[4]Edinburgh Ion Microprobe Facility, University of Edinburgh, Grant Institute, School of Geosciences, Edinburgh, EH9 3FE, UK.

Corresponding author email address: gleesonm1@cardiff.ac.uk

ABSTRACT

Despite their relatively low concentration in most oceanic basalts, volatile species (e.g. H_2O, CO_2 and S) have a disproportionately large influence on a wide range of mantle and magmatic processes. However, constraining the concentration of H_2O (and other volatiles) in basaltic magmas is not straightforward as submarine glass analyses are influenced by assimilation of hydrothermal brines, and the melt inclusion record is often reset by post-entrapment processes. Nevertheless, in this study we show that it is possible to reconstruct a detailed history of the volatile content of basaltic magmas through integration of multiple discreet volatile records and careful consideration of secondary processes. We present new analyses of volatiles in olivine-hosted melt inclusions, melt embayments and nominally anhydrous minerals (NAMS, clinopyroxene and orthopyroxene) found in basalts erupted on Floreana Island in the south-eastern Galápagos Archipelago. Our results indicate that the Floreana magmas, which are characterised by the most radiogenic Pb and Sr isotope signatures in the Galápagos Archipelago, contain H_2O concentrations between 0.4 and 0.8 wt% (at a melt Mg# of 0.65, where Mg# = Mg/(Mg + Fe) molar). These are marginally greater than the H_2O contents of magmas beneath Fernandina in the western Galápagos Archipelago (cf. 0.2–0.7 wt% H_2O at Mg# = 0.65). While the volatile content of magmas from the western archipelago follow trends

defined by concurrent mixing and crystallisation, NAMs from Floreana reveal the presence of rare, volatile-rich magmas (~2 wt% H_2O) that form as a consequence of reactive porous flow in mush-dominated magmatic systems beneath the south-eastern Galápagos. Furthermore, the Floreana magmas have similar H_2O/light Rare Earth Element ratios to basalts from the western Galápagos but contain F/Nd and Cl/K ratios that are ~2 – 3 times greater, indicating that the mantle source of the Floreana lavas might represent an important halogen reservoir in the Galápagos mantle plume.

1 INTRODUCTION

Magmatic volatiles (e.g. H_2O, CO_2 and S) have a major impact on mantle melting and rheology, crustal magma processing, and the timing and style of volcanic eruptions (Asimow et al., 2004; Asimow and Langmuir, 2003; Gaetani and Grove, 1998; Hirth and Kohlstedt, 2003, 1996; Stock et al., 2016). To advance understanding of magma system dynamics and mantle processes it is essential to place robust constraints on the volatile concentrations of magmas and their mantle source regions, as well as the behaviour of volatile species during magma ascent and eruption. In addition, in ocean island settings magmas are derived from melting in deep-sourced mantle plumes and deconvolving their volatile record offers a unique opportunity to study the volatile composition of recycled and primordial material stored in the Earth's lower mantle (Hofmann, 1997; White, 2010; Zindler and Hart, 1986).

Determining the pre-eruptive volatile content of silicate melts is complicated by the low-solubility of these components at low pressures (Dixon, 1997; Ghiorso and Gualda, 2015; Shishkina et al., 2014), which results in magma degassing during crustal storage, magma ascent, and cooling at the surface. The influence of low-pressure degassing on the H_2O and S contents of silicate melts can be mitigated by analysing the glassy exteriors of lava flows that are erupted under 100s to 1000s of metres of water, as the pressure of the overlying water column prevents significant loss of H_2O and S to the vapour phase (Dixon, 1997; Jackson et al., 2015; Peterson et al., 2017; Shimizu et al., 2016).

However, the volatile record preserved in submarine glasses is frequently complicated by post-eruptive hydration (Friedman and Long, 1976) and assimilation of Cl-rich brines during shallow magma storage and/or ascent (Kendrick et al., 2015; Le Roux et al., 2006). Consequently, many studies have instead focused on the use of melt inclusions to constrain magma volatile systematics (e.g. Cabral et al., 2014; Hartley et al., 2015; Koleszar et al., 2009; Métrich et al., 2014; Miller et al., 2019; Saal et al., 2002; Wieser et al., 2020). In theory, pockets of melt that are trapped within crystals are less likely to be affected by assimilation of Cl-rich components and might act as pressure vessels during magma ascent, inhibiting volatile degassing into a vapour phase (Lowenstern, 1995). Nevertheless, melt inclusions rarely provide a uncompromised record of magmatic H_2O or CO_2 at the time of entrapment -- due to the influence of decrepitation, post entrapment crystallisation, migration of volatile species into a vapour bubble and the geologically-fast diffusion of volatile species (primarily H_2O) through common crystal hosts, (Gaetani et al., 2012; Hartley et al., 2015; Maclennan, 2017; Steele-Macinnis et al., 2011). If secondary processes are carefully considered, however, melt inclusions and submarine glasses can still be used to evaluate magmatic volatile records.

To address the limitations of melt inclusion and submarine glass analyses, several studies have recently investigated the use of alternative methods for constraining magmatic volatile contents. For example, nominally anhydrous minerals (NAMs) incorporate volatiles as trace components, which can be related to the volatile contents of co-existing melts if the relevant Nernstian partition coefficients are known (Edmonds et al., 2016; Lloyd et al., 2016; Nazzareni et al., 2020; O'Leary et al., 2010; Turner et al., 2017; Wade et al., 2008). In addition, clinopyroxene crystals are less susceptible to low-pressure diffusive loss of H_2O than olivine-hosted melt inclusions (due to slower H_2O diffusivities; Costa et al., 2020; Ferriss et al., 2016; Turner et al., 2017), and might provide a more reliable record of pre-eruptive magma volatile contents. However, as erupted magmas often contain inherited (e.g. xenocrystic or antecrystic) material that did not form directly from their carrier liquid

(Gleeson et al., 2020a; Ubide et al., 2014; Wieser et al., 2019), detailed petrological characterisation is required to understand the relationship between the erupted crystal cargo and carrier melt before NAMs can be reliably interpreted to understand pre-eruptive magmatic volatiles.

In this study, we integrate published data from submarine glasses and melt inclusions with new analyses of melt inclusions, melt embayments (defined here as melt pockets that are partially enclosed by a host olivine crystal) and NAMs to: (i) determine the pre-eruptive concentration of volatile components such as H_2O and CO_2 for two well characterised regions of the Galápagos Archipelago that display highly contrasting eruptive styles (Floreana in the south-eastern archipelago and Fernandina in the western archipelago; Fig. 1; Allan and Simkin, 2000; Gleeson et al., 2020a; Harpp et al., 2014; Harpp and White, 2001; Koleszar et al., 2009; Peterson et al., 2017); (ii) identify how the volatile contents of each system evolve during magmatic differentiation; and (iii) place improved constraints on the volatile content of the Galápagos mantle plume. By combining these datasets and carefully considering the impact of secondary processes, we obtain a more comprehensive picture of the sub-volcanic volatile systematics than would be possible using any single petrological volatile record in isolation. In addition, our new data enable us to determine the impact of different mantle components on the volatile budget of ascending ocean island basalts (OIBs).

2 GEOLOGICAL SETTING

2.1 GEOCHEMICAL HETEROGENEITY IN THE GALÁPAGOS PLUME

The Galápagos mantle plume displays complex spatial heterogeneity in its trace element, isotopic and lithological composition (Geist et al., 1988; Gleeson et al., 2021; Gleeson et al., 2020b; Harpp and White, 2001; Hoernle et al., 2000; White et al., 1993). A minimum of 4 isotopic components intrinsic to the Galápagos plume are expressed in the geochemistry of erupted basalts across the archipelago, with at least three isotopically enriched mantle components (referred to as the PLUME

– high $^{3}He/^{4}He$; FLO – high $^{206}Pb/^{204}Pb$; and WD – high $^{207}Pb/^{206}Pb$ - components) identified in addition to an isotopically depleted eastern component (Harpp and White, 2001; Hoernle et al., 2000; White et al., 1993; Fig. 1). However, the simple spatial pattern of mantle heterogeneity in the Galápagos plume that has been identified through analyses of radiogenic isotope ratios, where enriched isotopic signatures are predominantly found in basalts from the southern and western Galápagos and isotopically depleted signatures are observed in the eastern Galápagos (Harpp and Weis, 2020), is complicated by the non-trivial relationship between isotopic and lithological heterogeneity (i.e., the presence of pyroxene-rich, and thus more fusible components in the Galápagos mantle plume; Gleeson and Gibson, 2019; Vidito et al., 2013). In fact, it has recently been proposed that a 'central pyroxenite' component is present in the mantle source region of volcanoes in the northern and central Galápagos, separating isotopically enriched signatures to the south-west from isotopically depleted signatures in the north-east (Gleeson et al., 2021).

The Floreana basalts have slightly elevated He isotope ratios (~11 R/R_A) compared to mid-ocean ridge basalts (MORBs; ~8 R/R_A) and radiogenic Sr and Pb isotope signatures relative to basalts erupted in other regions of the Galápagos Archipelago ($^{206}Pb/^{204}Pb$ ~19.55–20.06 and $^{87}Sr/^{86}Sr$ ~0.70325–0.70359; Harpp et al., 2014; Harpp and White, 2001; Kurz and Geist, 1999). They are also characterised by high light-to-middle rare earth element (REE) ratios, but low middle-to-heavy REE ratios, resulting in a notable concave up REE signature (Harpp et al., 2014). In contrast to Floreana, basalts erupted on or near Fernandina typically have unradiogenic He and Ne isotope signatures ($^{3}He/^{4}He$ ~29 R/R_A; $^{20}Ne/^{22}Ne$ ~12.5 at $^{21}Ne/^{22}Ne$ ~0.034; Kurz et al., 2009) and moderately radiogenic Sr and Pb isotope signatures ($^{206}Pb/^{204}Pb$ ~19.10 and $^{87}Sr/^{86}Sr$ ~0.70325; Harpp and White, 2001; Peterson et al., 2017; Saal et al., 2007).

2.2 Variations in melt flux, geomorphology and eruptive styles

The islands of Fernandina and Floreana are characterised by contrasting volcanic morphologies and eruptive styles (Allan and Simkin, 2000; Bow and Geist, 1992; Harpp et al., 2014; Harpp and Geist,

2018; Lyons et al., 2007). Fernandina is located near the centre of the postulated Galápagos plume stem, whereas Floreana is ~100 km downstream (i.e. in the direction of Nazca plate motion; Fig. 1; Hooft et al., 2003; Villagómez et al., 2014). As a result, the flux of magma into the lithosphere beneath Fernandina is substantially greater than beneath Floreana, which is manifest in a volumetric eruption rate at least six orders of magnitude greater at Fernandina (Harpp et al., 2014; Poland, 2014).

Unlike other Galápagos islands, Floreana magmas are predominantly stored in the lithospheric mantle (at ~24 km depth; Gleeson et al., 2020a). Additionally, there is a high proportion of pyroclastic material on Floreana (relative to the volume of effusive lavas) compared to the other Galápagos islands, and the deposits contain an unusual abundance of mafic and ultramafic xenoliths (Harpp et al., 2014; Lyons et al., 2007). These features have been interpreted as evidence for rapid magma ascent rates, which might result from high volatile concentrations in Floreana primary melts (Harpp et al., 2014). However, while this hypothesis is consistent with many of the volcanological features on Floreana, no analytical constraints currently exist on the volatile contents of magmas beneath the island.

The comparatively high flux of magma into the lithosphere beneath Fernandina has resulted in development of a magmatic storage region in the mid- to lower-crust, which is characterised by both crystal-rich and melt-rich regions, and the formation of a single volcanic edifice with a large central caldera (Allan and Simkin, 2000; Geist et al., 2014, 2006). Although localized, small, compositionally diverse melts have been evidenced in the crust (i.e., the presence of melts of andesitic – dacitic compositions), the high flux of magma into the Fernandina sub-volcanic system efficiently buffers the mean composition of erupted magmas (Geist et al., 2014; Stock et al., 2020). Both subaerial and submarine eruptions on Fernandina are typically effusive, with basaltic lava flows originating from either circumferential or radial fissures (Chadwick et al., 2011; Vasconez et al., 2018).

3 METHODOLOGY

3.1 SAMPLES AND PREPARATION

Melt inclusions, embayments, matrix glass and nominally anhydrous minerals (clinopyroxene and orthopyroxene) were analysed from a single sample (17MMSG16) of fresh scoria lapilli (total volume of ~200-500 cm^3, individual scoria fragments typically 0.5–1.5 cm diameter) that was collected from the base of an emergent scoria cone on the northern coast of Floreana (Punta Cormorant; 90.42752°W, 1.22495°S; Fig. 1). The scoria is olivine phyric with minor clinopyroxene (<5 vol% of crystals) and very rare orthopyroxene (<<1 vol%). Clinopyroxene crystals were also analysed from 3 wehrlite, 2 dunite, and 2 gabbroic xenoliths (2–10 cm across), collected from scoria cones on the northeast coast of Floreana (Fig. 1). Prior to geochemical analysis, the scoria and xenolith samples were crushed, and crystals hand-picked from the 0.25–0.5 and 0.5–1 mm size fractions.

Olivine-hosted melt inclusions are very rare in the Floreana scoria and are typically found in small crystals (0.25–0.5 mm long axis). Where present, there are often multiple inclusions or embayments in a single host crystal, which have been quenched on eruption. Although most melt inclusions are smaller (<10 µm) than the beam size (~20 µm) used during secondary ion mass spectrometry (SIMS), the largest inclusions are analysable, extending to ~20–50 µm diameter (Fig. 2). Olivine crystals that contain melt inclusions and/or embayments were mounted individually in CrystalBond™ and hand polished until the glass was exposed at the surface. Once the melt inclusions and embayments were exposed, the crystals were removed from the CrystalBond™, mounted in epoxy resin and a final polish was applied. Clinopyroxene and orthopyroxene crystals that were separated from the Floreana scoria or xenoliths for NAM analyses were also mounted individually in CrystalBond™ and hand polished. After polishing, clinopyroxene and orthopyroxene crystals were removed from the CrystalBond™ and hand pressed into indium metal (at ~120°C to soften the metal). The mounts were then flattened using a hydraulic press to ensure a flat sample surface for analysis.

Prior to Secondary Ion Mass Spectrometry (SIMS) and Electron Probe Microanalysis (EPMA), Backscatter Electron maps were created for all sample mounts, and images were taken of individual crystals, using a Field Emission Gun Scanning Electron Microscope (Quanta-650F) at the University of Cambridge (Fig. 2). Mapping was carried out in low vacuum mode (as samples were uncoated) using a ~5 nA beam current and a 20 kV accelerating voltage. To mitigate the risk of electron-beam induced sample damage (Humphreys et al., 2006) or contamination from C coating, volatiles (CO_2, H_2O, F, and Cl) were analysed in the Floreana glasses and NAMs by SIMS prior to exposure to a focused electron beam (EPMA).

3.2 SECONDARY ION MASS SPECTROMETRY (SIMS)

All glass (that is, matrix glasses, melt inclusions and melt embayments) and NAM samples were Au coated and analysed using a Cameca ims-4f instrument at the Edinburgh Ion Microprobe Facility (EIMF; University of Edinburgh). The NAM sample mounts were loaded into the instrument vacuum chamber and pumped down for 3 days prior to analysis to reduce H_2O background count rates. All analyses were performed with a 14.5 keV $^{16}O^-$ primary beam and a positive secondary ion beam. A liquid N_2 cold trap was attached to reduce background ^1H counts.

Glass volatile and trace element concentrations were measured using two separate SIMS protocols. Carbon was analysed first, using a 5 nA primary ion beam at high mass resolution (~1200 M/ΔM) to avoid $^{24}Mg^{2+}$ interference, a 3 min pre-sputter rastering over a 30 μm^2 area, and a secondary ion energy filter of 50 ±25 V. ^{12}C backgrounds were determined via regular analysis of the host olivines and were between 1 and 4 cps (counts per second), which was subtracted from each analysis prior to calculation of sample CO_2 concentrations. Water, F, Cl and other trace elements were measured in a second analysis of the same spot at lower mass resolution (~300 M/ΔM), using a 5 nA primary beam, an energy offset of 75 ±25 V, and a ~2 min pre-sputter with a 30 μm^2 raster area. ^1H backgrounds were determined through analysis of olivine crystals that host melt inclusions and/or embayments. Background measurements were carried out several times during the analytical

session and were typically between 1100 and 1700 cps (corresponding to apparent H_2O concentrations between 0.05 and 0.07 wt%). The background count rate was subtracted from the measured cps of each analysis prior to calculation of the measured H_2O concentration. As the Floreana olivines are expected to contain only 10-20 ppm H_2O (calculated using the partition coefficients for water ($D^{H2O}_{olivine\text{-}melt}$) of Hauri et al. (2006) and the measured concentration of H_2O in the olivine-hosted melt inclusions), these background measurements are uninfluenced by the trace amounts of H_2O that may be held in the olivine structure.

Nominally anhydrous mineral H_2O concentrations were measured using a 5 nA primary beam, with a 6 min pre-sputter rastered over 30 μm^2 to remove any H_2O adsorbed onto the sample surface. Alongside ^{1}H, the isotopes ^{19}F, ^{26}Mg, ^{27}Al, ^{30}Si, ^{35}Cl, ^{39}K, ^{44}Ca and ^{47}Ti were also measured and were used to detect whether any standard analyses differed from their published values. Only high-energy secondary ions with an energy of 75 ±25V were allowed in the mass spectrometer. An effective field aperture of 8 µm was used to further reduce ^{1}H backgrounds. ^{1}H backgrounds were evaluated using the reference material CPX SMC31139 (Kumamoto et al., 2017), which contains 5 ppm H_2O, as well as an olivine separated from the scoria of sample 17MMSG16. Repeat analyses of CPX SMC31139 indicates that the ^{1}H backgrounds are between 1 and 7 cps (equivalent to 2-15 ppm H_2O). Notably, these low background count rates indicate that the olivine of sample 17MMSG16 has 12±2 ppm H_2O (n=4), consistent with the H_2O contents estimated based on our melt inclusions analysis for sample 17MMSG16 and published values of $D^{H2O}_{olivine\text{-}melt}$ (Hauri et al., 2006).

Laser Ablation Inductively Coupled Plasma Mass Spectrometry (LA-ICP-MS) analysis of the trace element composition of the clinopyroxene crystals analysed in this study were presented in Gleeson et al. (2020a). The LA-ICP-MS analyses were located directly on top of the much smaller SIMS pits.

For glasses, H_2O and CO_2 concentrations were calculated from working curves of $^{1}H/^{30}Si$ and $^{12}C/^{30}Si*SiO_2$ produced using well-characterised basaltic glass standards (N72, M40, M10, and M36; Shishkina et al., 2010). Fluorine was calibrated against BCR-2g, whereas Cl and the other trace

elements were calibrated against GSD-1G (Marks et al., 2017), with ^{30}Si as an internal standard. Middle REE and heavy REE were corrected for light $REE^{16}O$ or BaO interferences using predetermined oxide production rates, whereas ^{85}Rb was corrected for $^{56}Fe^{29}Si$ calculated from $^{56}Fe^{28}Si$ measured on mass 84 (after correcting for isobaric ^{84}Sr) using in-house ION6 software.

Clinopyroxene volatile contents are underestimated when they are calculated from basaltic glass $^{1}H/^{30}Si$ working curves, due to different ion beam sputtering rates in the different matrices (i.e. matrix effects; Kumamoto et al., 2017; Supplementary Information). Consequently, the H_2O analyses were calibrated using recently-characterised clinopyroxene and orthopyroxene standards (only analyses that returned major element concentrations similar to the published values were used in the calibration slope; Kumamoto et al., 2017; Supplementary Information). Standards were analysed at regular intervals to check for instrument drift and to maintain the best-possible calibrations.

The precision of SIMS analyses were tracked through repeat analysis of a microlite-free basaltic glass from Wolf volcano (Galápagos; sample 17MMSG39 of Stock et al., 2018) for H_2O, F, and Cl, standard material M40 (Shishkina et al., 2010) for CO_2 and BCR-2g for other trace elements. Typical 2σ precision is ~10%, ~4%, ~7% and ~5% for H_2O, F, Cl and CO_2, respectively, and ~4–6% for other trace elements, except Nd (~10%) and the heavy REE (Tm, Yb, Lu; <20%). The 2σ precision of NAM H_2O analyses were determined through repeat analysis of homogeneous clinopyroxene cores from Floreana sample 17MMSG16 (~10%) and repeat analysis of secondary standard materials (e.g. ALV-519-4-1; ~8%). Analytical recovery was determined through repeat analysis of a clinopyroxene standard (CPX-KH04-4; 90–105%, with an average recovery value of 100%; Kumamoto et al., 2017).

3.3 Electron Probe Microanalysis (EPMA)

Following SIMS analysis, the samples were briefly re-polished (to remove the Au coat) and C coated. Glasses and clinopyroxenes were analysed for major (>1 wt%) and minor elements (<1 wt%) using a Cameca SX100 electron microprobe in the Department of Earth Sciences, University of Cambridge. Analytical routines and standard data for clinopyroxene and orthopyroxene analyses are reported in

Gleeson et al. (2020a) where EPMA spots were located as close as possible to the SIMS pits. For glass analyses, spots were also placed close to the SIMS pits and the EPMA was calibrated with appropriate mineral and metal standards (see Gleeson and Gibson, 2019 for details). Glass analyses were collected using a 6 nA, 15 kV, defocused (5 µm) beam. Sodium and K were analysed first (10s peak count time) to avoid alkali migration during electron beam exposure. Other elements were analysed with peak count times of 10s (Si), 20s (Fe), 30s (Al, P, Ca, Mg), 40s (Mn), or 60s (Ti; backgrounds were determined by counting for half the peak count time on either side of the peak). Sulphur was analysed last using a 20 nA beam and a 60s peak count time.

Analytical uncertainties were tracked through analysis of the VG2 standard material (Jarosewich et al., 1980). Typical 2σ precision is <3% for major elements and <5-10% for minor elements. Analytical recovery was also measured through repeat analysis of VG2 (Jarosewich et al., 1980) and is typically 98–102% for all elements.

4 RESULTS

4.1 MELT INCLUSIONS, EMBAYMENTS AND MATRIX GLASSES

In total, 25 olivine-hosted melt inclusions and embayments, and 13 matrix glasses were analysed from sample 17MMSG16 (Supplementary Data). A high proportion of olivine crystals in 17MMSG16 are xenocrystic and no melt inclusions or embayments were identified in these crystals; all melt inclusion analyses in this study are from the autocrystic crystal population identified by Gleeson et al. (2020a), which is characterised by relatively high Ca contents in the olivine (>1500 ppm).

4.1.1 Major and trace elements

The basaltic glasses analysed in this study typically plot above the alkali-tholeiite divide on a total alkali versus silica plot, straddling the transition between basalts and trachy-basalts (Fig. 3; Irvine and Baragar, 1971). They have higher total alkali contents ($Na_2O + K_2O$ ~4–6 wt%) than the Floreana whole-rock data (Harpp et al., 2014), but are comparable to previously-published matrix glass

analyses (Gleeson et al., 2020a). The melt inclusions and embayments have a similar range of FeO_t contents to the Floreana whole-rock (~ 8 – 10.5 wt%) and are in Mg-Fe disequilibrium with their olivine hosts (i.e., melt inclusion glass Mg#, where Mg# = Mg/(Mg + Fe_t) molar, are typically lower than expected based on the composition of the host olivines; Supplementary Information). As the similar range of melt inclusions and whole-rock FeO_t contents indicates that there is no clear Fe-loss during Post-Entrapment Crystallisation (PEC), we estimate the extent of PEC by adding back in the host olivine composition to each melt inclusion until olivine-melt equilibrium is achieved (assuming a K_d of 0.30 and a Fe^{3+}/Fe_{tot} ratio of 0.15; Roeder and Emslie, 1970). These calculations indicate that each of the Floreana melt inclusions has undergone <10% PEC. However, the large uncertainty in the FeO_t content of the original trapped Floreana melts (8 – 10.5 wt% FeO_t), precludes accurate corrections for the chemical changes that occur during PEC (cf. Wieser et al., 2020). As a result, we use the measured melt inclusion compositions rather than the PEC corrected compositions in the following discussions.

The analysed glasses from Floreana are characterised by high concentrations of fluid mobile trace elements (e.g. Rb, Ba, K; Fig. 4) and moderately high concentrations of high field-strength elements (e.g. Ti, Ta, Nb) relative to the Fernandina lavas of the western Galápagos (Floreana glasses in this study have mean Ba and Nb contents of ~310 ppm and ~25 ppm, respectively, relative to Fernandina glass contents of Ba ~91 ppm and Nb ~23 ppm – data from Peterson et al., 2017). In addition, the Floreana glasses have concave-up rare-earth element (REE) patterns, with high light REE/middle REE ratios (e.g. $[La/Sm]_n$) and relatively low middle REE/heavy REE ratios (e.g. $[Sm/Yb]_n$) compared to basalts from the western Galápagos, in agreement with previous geochemical data from Floreana (Fig. 4). Notably, the deviation between the PEC-corrected trace element (and volatile element) data is typically smaller than the error associated with SIMS analysis, so the measured values are used in all discussions below.

4.1.2 Volatile elements

Substantial heterogeneity is observed in the volatile element concentrations of the Floreana glasses, with embayments containing lower concentrations of S and H_2O (~100-1000 ppm and 0.05 – 0.35 wt%, respectively) than the melt inclusions (~1250 ppm S and 0.54 – 0.77 wt% H_2O; Fig. 5). A positive correlation is observed between the H_2O and S concentrations of the Floreana glasses (Fig. 5 & 6). The CO_2 concentrations measured in the melt inclusions range from ~700 to ~8800 ppm, whereas the CO_2 concentration of the melt embayments are consistently $\lesssim$2000 ppm (Fig. 5).

The F and Cl concentrations of the Floreana melt inclusions and melt embayments range between 458–962 ppm and 360–1144 ppm, respectively. These exceed the concentrations of F and Cl previously measured in melt inclusions (1–170 ppm Cl) and submarine glasses (376–561 ppm F) from Fernandina in the western Galápagos (Fig. 7; Koleszar et al., 2009; Peterson et al., 2017). There is no correlation between the halogen contents of the Floreana glasses and their H_2O or S contents. However, correlations are observed between Cl and other highly incompatible trace elements, such as Ba, Nb and K (Fig. 6).

4.1.3 Volatile/non-volatile trace element ratios

Volatile to non-volatile trace element ratios that are unfractionated during mantle melting and crystallisation (owing to their similar bulk partition coefficients) are commonly used to assess the volatile content of primary mantle melts and their mantle source regions (Cabral et al., 2014; Gibson and Richards, 2018; Jackson et al., 2015; Métrich et al., 2014; Peterson et al., 2017; Saal et al., 2002; Shimizu et al., 2016). Additionally, knowledge of the primary volatile to non-volatile trace element ratios in a system can facilitate calculation of 'original' melt volatile concentrations, prior to secondary processing (e.g. degassing and diffusive volatile loss; Hartley et al., 2015; Saal et al., 2002).

We use the ratios H_2O/La, F/Nd and Cl/K (and Cl/Nb), which are hypothesised to remain constant during mantle melting and fractional crystallisation, to investigate variations in the volatile systematics of the Galápagos basalts (Lassiter et al., 2002; Peterson et al., 2017; Rosenthal et al.,

2015; Saal et al., 2002). We primarily consider the H_2O/La ratio of the Galápagos basalts, instead of the more commonly used H_2O/Ce ratio, to interrogate their pre-eruptive H_2O contents as recent experimental data indicate that the partitioning behaviour of H_2O more closely resembles that of La rather than Ce (see Supplementary Information; Rosenthal et al., 2015). The experimental data for F partitioning is less clear, with some studies indicating that it has a similar behaviour to La during mantle melting (Rosenthal et al., 2015), whereas others suggest that it has a similar compatibility to Pr or Nd (Dalou et al., 2012; Kendrick et al., 2017). Therefore, owing to the uncertainty in the partitioning of F during mantle melting we consider the ratio F/Nd, as this is the most frequently used in the literature, to investigate the F contents of the Galápagos basalts and their mantle source regions. We do, however, acknowledge that variations in the average melt fraction of the Galápagos mantle could lead to changes in the F/Nd ratio of the erupted basalts if F is less compatible than Nd, as indicated by the study of Rosenthal et al. (2015). CO_2/Nb and CO_2/Ba ratios are not considered in this study, owing to the strong degassing control on the CO_2 content of the Floreana magmas (see Section 5); this decouples CO_2 from trace elements with similar bulk partition coefficients during mantle melting.

Considerable variability is observed in the H_2O/La (45–550), F/Nd (29–47.5) and Cl/K (0.062–0.124) ratios of the Floreana melt inclusions and embayments (Fig. 7). The Floreana melt inclusion F/Nd ratios extend to considerably higher values than the F/Nd ratio of basalts from the western Galápagos (~21; Peterson et al., 2017). In addition, the Cl/K ratio of Floreana glasses are higher than those of most unaltered/uncontaminated OIBs and MORBs (i.e. 0.01–0.08; Kendrick et al., 2015; Le Roux et al., 2006; Michael and Cornell, 1998), but are similar to the values measured in basaltic melt inclusions from HIMU ocean-island basalts (i.e. Mangaia and Rairua; Hanyu et al., 2019). The Cl/Nb ratio of the Floreana glasses are also higher than most previously measured unaltered MORBs and OIBs, including the Cl-rich HIMU localities (Floreana Cl/Nb ~ 32.9 ±13.1; Mangaia Cl/Nb <15; Hanyu et al. 2019).

4.2 NOMINALLY ANHYDROUS MINERALS

We collected H_2O data from five clinopyroxene and one orthopyroxene crystals from scoria sample 17MMSG16 (28 individual analyses in total), as well as clinopyroxene crystals separated from 3 wehrlite (7 crystals and 17 individual analyses; 17MMSG02b, 17MMSG02c, 17MMSG03a), 2 dunite (3 crystals and 7 individual analyses; 17MMSG04c, 17MMSG04f), and 2 gabbro xenoliths (6 crystals and 17 individual analyses; 17MMSG03b, 17MMSG04b). SIMS analyses were carried out on the core and rim of each crystal (from both the scoria and xenolith samples) to characterise the variability in H_2O concentrations across an individual grain. In addition, a small number of core-to-rim profiles were also collected on the scoria clinopyroxene crystals (Fig. 2; Supplementary Information).

Equilibrium melt H_2O concentrations can be calculated from clinopyroxene and orthopyroxene H_2O concentrations through the application of Nernstian H^+ partition coefficients ($D_H^{pyroxene-melt}$). As the main incorporation mechanism of hydrogen into pyroxene is through the heterovalent coupled substitution $^{IV}Si^{4+} = {}^{IV}Al^{3+} + H^+$, the main control on $D_H^{pyroxene-melt}$ in natural magmatic systems is thought to be the concentration of tetrahedrally coordinated Al^{3+} (O'Leary et al., 2010; Turner et al., 2017). Clinopyroxene major element compositions, taken from Gleeson et al. (2020a) for each individual SIMS analysis, are used to calculate $D_H^{clinopyroxene-melt}$ and $D_H^{orthopyroxene-melt}$ using the experimentally-calibrated, temperature-independent parameterisations of O'Leary et al. (2010). Calculated $D_H^{pyroxene-melt}$ values are in the range 0.010 –0.027, and we obtain similar results using other parameterisations (Novella et al., 2014; Turner et al., 2017).

4.2.1 Scoria crystals

Clinopyroxene crystals from scoria sample 17MMSG16 have H_2O contents between 20 and 350 ppm. In crystals where multiple core analyses were performed, relatively homogeneous core H_2O concentrations were observed (<10% variability) with lower H_2O contents, by ~10-40%, at their rims (Fig. 2). While this suggests that low pressure degassing has caused diffusive loss of H_2O from crystal rims, the relatively homogeneous nature of the crystal cores indicates that diffusive loss of H_2O

during low pressure degassing has a very small influence on these core H_2O concentrations. Equilibrium melt H_2O concentrations calculated from the analyses of the pyroxene cores are typically between 0.30 and 0.80 wt% but extend up to ~1.6 wt% (partition coefficients calculated using the T-independent parameterisation of O'Leary et al. 2010).

4.2.2 Xenoliths

Clinopyroxene crystals in the wehrlitic and dunitic xenoliths have H_2O concentrations between ~60 and 310 ppm, similar to the range of H_2O contents observed in clinopyroxene crystals from the scoria. Multiple analyses of each crystal indicate that the H_2O concentration of a single crystal is typically constant (including both core and rim analyses). There is, however, one notable exception; in crystal 2 from sample 17MMSG03a the measured H_2O concentrations vary from ~62 ppm to ~259 ppm (lowest H_2O concentrations are observed near the crystal rim), potentially indicating that this crystal was influenced by incomplete diffusive re-equilibration with a relatively H_2O-poor carrier melt. Using the T-independent parameterisation for H_2O partitioning into clinopyroxene from O'Leary et al. (2010), equilibrium-melt H_2O contents can be determined for each of the clinopyroxene crystals. In the wehrlitic and dunitic xenoliths, the clinopyroxene analyses indicate a range of equilibrium melt H_2O concentrations between ~0.35 and ~1.8 wt%.

The H_2O concentrations measured within clinopyroxene crystals from each of the two gabbroic xenoliths analysed are relatively constant for each sample (209 ±47 ppm (n=7) and 151 ±29 ppm (n=10) - 2σ variation). Calculation of equilibrium melt H_2O concentrations indicates that these xenoliths last equilibrated with melts containing 1.19 ±0.13 and 0.64 ±0.12 wt% H_2O, respectively.

5 DISCUSSION

5.1 VOLATILE SYSTEMATICS IN THE SOUTH-EASTERN GALÁPAGOS ARCHIPELAGO

5.1.1 Floreana melt inclusion entrapment pressures

The solubility of CO_2 in basaltic magmas is highly sensitive to the pressure of magma storage (Dixon, 1997; Ghiorso and Gualda, 2015; Shishkina et al., 2014). However, using melt inclusion CO_2 contents to estimate magma storage pressures is complicated by post-entrapment processes, such as decrepitation (Maclennan, 2017) or migration of CO_2 into a vapour bubble (Steele-Macinnis et al., 2011; Wieser et al., 2020). Nevertheless, while these post-entrapment processes act to decrease the CO_2 content of the melt inclusion glass, analysis of the melt phase still permits estimation of minimum entrapment pressures, which can be compared to other barometric estimates.

The apparent entrapment pressures of the Floreana melt inclusions were calculated in the Python library VESIcal (Iacovino et al., 2020; Wieser et al., 2021) using the H_2O-CO_2 solubility models of Ghiorso and Gualda (2015), Iacono-Marziano et al. (2012) and Shishkina et al. (2014). These models are all calibrated on datasets that overlap with the major element composition of the melt inclusions in this study and return calculated entrapment pressures that are in close agreement (typically <10 % difference; see Supplementary Information). In detail, our Floreana melt inclusions return minimum entrapment pressures ranging from ~100 MPa to ~720 MPa, with >50% of inclusions giving minimum entrapment pressures >450 MPa, consistent with the mineral-melt thermobarometry of Gleeson et al. (2020a; 717 ±165 MPa). Although ~70% of the inclusions in our samples contain visible vapour bubbles, our highest calculated entrapment pressure (~720 MPa) is from a bubble free inclusion. Additionally, we note that high melt inclusion entrapment pressures (>450 MPa) were obtained from both bubble free and bubble-bearing melt inclusions, indicating that most of the CO_2 within these bubble-bearing melt inclusions is likely held in the melt phase, consistent with the low extents of PEC estimated above (Wieser et al., 2020).

5.1.2 Degassing and diffusive controls on H_2O, S and CO_2

Water is more soluble than CO_2 in basaltic melts and OIB magmas are therefore unlikely to degas substantial amounts of H_2O until they reach very low pressures, likely within the upper ~1 km of crust (Dixon, 1997; Ghiorso and Gualda, 2015; Shishkina et al., 2014). Nevertheless, rapid diffusion of H_2O (or H^+ ions) in silicate melts and minerals during magma storage, differentiation and ascent can lead to substantial variability in melt inclusion and embayment H_2O concentrations and H_2O/La ratios.

The large range of H_2O concentrations (0.05–0.77 wt%) and H_2O/La ratios (~45–550; Fig. 7) in Floreana melt inclusions and embayments cannot result from magma degassing prior to melt inclusion or melt embayment formation as melt inclusion CO_2 concentrations and mineral-melt thermobarometry indicate high pressure storage (Gleeson et al. 2020a). Instead, these data can be explained though a simple petrogenetic model whereby: (i) melt inclusions with variable H_2O contents are trapped in olivine crystals that settle into a cumulate mush; (ii) this mush is disaggregated shortly prior to eruption and olivine crystals (containing melt inclusions and/or embayments with diverse geochemical compositions) are entrained into a carrier liquid with a different H_2O content to the trapped melts; (iii) owing to the gradient in H_2O concentrations between the trapped and external melt, H^+ diffusion drives re-equilibration of the melt inclusion H_2O contents with the external melt phase in a matter of hours (Hartley et al., 2015); (iv) syneruptive degassing of H_2O from the carrier melt at low pressures drives diffusion of H_2O out of the melt embayments and inclusions, potentially reducing the final H_2O concentration measured in the melt embayments and some melt inclusions (Fig. 5). The extent of H_2O loss from the melt embayments and inclusions during this final step of the model will be controlled by a number of different factors, including: their initial water contents; the magma ascent rate; the size and shape of the embayment/inclusions and host crystal; and the temperature of the system (Barth et al., 2019; Ferguson et al., 2016; Gaetani et al., 2012).

441 The influence of low pressure degassing on the volatile content of the Floreana melt embayments
442 can be evaluated by modelling magma degassing and diffusive loss of H_2O, CO_2 and S through an
443 elongate channel during magma ascent and eruption, i.e. an embayment (Fig. 5; Ferguson et al.,
444 2016). To do this, we simulate embayment formation and isothermal magma decompression using a
445 range of starting pressures (250–750 MPa), ascent rates (0.005–0.5 MPa/s), termination pressures
446 (0.1–0.3 MPa), and initial water contents (0.55–0.95 wt%) at constant initial S (1250 ppm). Diffusive
447 transport of H_2O, CO_2, and S along the modelled embayment was evaluated at 5 µm increments in
448 embayments of various lengths (100 – 500 µm). At each model step the concentrations of H_2O, CO_2
449 and S in the carrier melt were calculated using the solubility model of Ghiorso and Gualda (2015;
450 MagmaSat) for H_2O and CO_2 and Witham et al. (2012; SolEx) for S. These volatile contents were then
451 used to define the outer boundary condition for the diffusion models. Volatile diffusion within the
452 melt embayments was then modelled following the method of Ferguson et al. (2016), with H_2O and
453 CO_2 diffusivities in basaltic melts from Zhang and Ni (2010), and S diffusivities from Zhang et al.
454 (2010).

455 The results of our simple diffusion models provide important insights into the volatile content of
456 magmas beneath Floreana. For example, they indicate that the H_2O vs S trend in the Floreana
457 embayments can be reproduced when the initial H_2O content of the system is between 0.55 and
458 0.75 wt%, corresponding to the range in H_2O contents measured in our melt inclusions (Fig. 5). In
459 addition, the diffusion models also recreate the H_2O vs CO_2 systematics of the Floreana melt
460 embayments (Fig. 5).

461 We do not use our diffusion models to estimate the decompression rate of the Floreana magmas, as
462 we were not able to collect transects along individual embayments (owing to their narrow width and
463 the relatively large spot size of our analyses; Lloyd et al., 2014), and so our measurements typically
464 represent a single analysis from each embayment. In addition, the embayments analysed in this
465 study display a range of morphologies, which will influence the diffusion of volatile species out of the

466 embayments and complicate any estimates of decompression rates based on the simple one-
467 dimensionaldiffusion modelling (deGraffenried and Shea, 2021). Nevertheless, as indicated above,
468 these coupled decompression-diffusion models for a simple melt embayment demonstrate that the
469 volatile contents of the Floreana embayments are closely reproduced when the initial H_2O contents
470 are within the range measured in our Floreana melt inclusions (~0.55–0.75 wt%). This observation is
471 critical as it indicates that the Floreana melt inclusions re-equilibrated their H_2O contents with the
472 carrier melt prior to eruption and thus record the pre-eruptive carrier melt H_2O content. This
473 hypothesis is consistent with the geologically fast diffusion of H^+ through the olivine lattice driving
474 rapid pre-eruptive re-equilibration of melt inclusion H_2O contents with the external carrier melt (see
475 step (iii) of the petrogeneic model above; Gaetani et al., 2012; Hartley et al., 2015).

476 Therefore, taking our measured matrix glass La contents and the H_2O content of our melt inclusions
477 (i.e. assuming that melt inclusions have diffusively re-equilibrated with the carrier liquid prior to
478 eruption), we can estimate the H_2O/La ratio of the pre-eruptive Floreana magma. By doing so, we
479 can constrain the pre-eruptive melt H_2O/La ratio to ~270–370, consistent with the H_2O/La content
480 measured in a submarine glass sample collected on the flanks of Floreana and analysed by Peterson
481 et al. (2017; sample DRIFT04 D69b, H_2O/La ~350). Importantly, this submarine glass has a radiogenic
482 Pb isotope composition that is similar to the Floreana subaerial basalts and, therefore, is likely
483 derived from the same magmatic system (Peterson et al., 2017).

484 The Cl/K and Cl/Nb ratios of Floreana submarine glass sample DRIFT04 D69b (0.100 and 28.6,
485 respectively; Peterson et al., 2017) also closely match those measured in our melt inclusions and
486 embayments (0.096 ±0.030 and 32.9 ±13.1). Additionally, the correlation between Cl and
487 incompatible trace elements such as Ba, Nb, and K in the Floreana melt inclusions and embayments
488 indicates that the Cl concentrations of these glasses, and by extension their H_2O concentrations, are
489 not influenced by assimilation of a Cl-rich component (e.g. a hydrothermal brine; Kendrick et al.,
490 2015). As such, the similarity between the H_2O/La ratio of Floreana submarine glass DRIFT04 D69b

and that estimated from our melt inclusion and embayment analyses supports the interpretation that our measured melt inclusion H_2O concentrations are representative of the pre-eruptive carrier melt H_2O concentration.

5.1.3 Heterogeneity in sub-volcanic H_2O concentrations

Previous work on the isotopic composition of cumulate xenoliths from Floreana indicate that gabbroic xenoliths found in the scoria and lava deposits are isotopically similar to present-day lavas erupted at Sierra Negra and Cerro Azul volcanoes in the western Galápagos, proximal to the Galápagos plume stem (Fig. 1; Lyons et al., 2007). Consequently, gabbroic xenoliths, and scoria crystals that are chemically similar to the gabbroic clinopyroxenes (17MMSG16 crystal 4; Gleeson et al., 2020a), are interpreted to represent ancient remnants of an earlier period of volcanic activity on Floreana (>1.5 Ma), before Nazca plate motion carried the island away from the centre of Galápagos plume upwelling (Lyons et al., 2007). In contrast, wehrlite and dunite xenoliths have isotopic signatures analogous to recent Floreana lavas and are interpreted to be fragments of the present-day magmatic system (<1–1.5 Ma; Lyons et al. 2007). As a result, the volatile data collected from clinopyroxene crystals in the Floreana scoria and cognate xenoliths provide a unique insight into the H_2O concentrations of basaltic magmas in the south-eastern Galápagos and, through the >1.5 Ma gabbroic xenoliths, the western Galápagos Archipelago. Furthermore, because clinopyroxene crystals from the scoria samples are often derived from liquid-rich magma storage regions and wehrlite and dunite xenoliths are derived from crystal-rich mush zones (Gleeson et al., 2020a), the analysis of NAMs in these different sample types can be used to reconstruct the volatile content of basaltic magmas in different parts of the present day magmatic system (Fig. 8).

The yellow field on the right-hand axis of Figure 8 shows a kernel density distribution of melt H_2O contents in equilibrium with NAM analyses that are uninfluenced by diffusive loss of H_2O during low pressure degassing (i.e., excluding rim analyses that return H_2O contents >>10% lower than the respective crystal core) and are derived from the present-day Floreana magmatic system (i.e. those

that show no chemical affinity to the gabbroic xenoliths). The kernel density distribution has a primary peak at ~0.4–0.8 wt% H_2O, with a long tail to high equilibrium-melt H_2O contents and a secondary peak at ~1.5 wt% H_2O. In addition, a kernel density distribution was also constructed for the melt H_2O concentrations predicted from the Floreana whole-rock data, using the measured La concentrations (Harpp et al., 2014) and an assumed melt H_2O/La ratio of 350 (grey field in Fig. 8). While we acknowledge that there might be small differences in the true H_2O/La of the Floreana basalts, the kernel density distribution of melt H_2O concentrations predicted from these whole-rock analyses display several similarities with that constructed for the NAMs from the present-day magmatic system, with a primary peak at ~0.4–0.8 wt% H_2O and a tail to higher H_2O contents (1–2 wt%; Fig. 8).

The overlap between the primary peaks in the two kernel density distributions validates our calculated equilibrium melt H_2O concentrations from the NAMs and likely records the typical range of pre-eruptive melt H_2O concentrations in the present-day Floreana magmatic system (0.4–0.8 wt% H_2O). This is further supported by the similarity between the location of the kernel density distribution primary peaks and the H_2O concentrations measured in our Floreana melt inclusions (0.54–0.77 wt%). However, the subsidiary peak in the NAM equilibrium-melt kernel density distribution and melt H_2O concentrations predicted from the whole-rock data record substantially higher melt H_2O contents than our Floreana melt inclusions or embayments (Fig. 8).

There are two potential origins for the anomalously H_2O-rich (and trace element enriched) melts identified from the Floreana NAMs and whole-rock data: (i) they formed from low-fraction mantle melts generated at the base of the melting region and have incompletely mixed with H_2O-poor melts produced at shallower depths; or (ii) they derive from magmas that have undergone chemical enrichment via reactive porous flow (that is, disequilibrium melt-mush reaction during melt transport) or *in-situ* crystallisation in highly-crystalline storage regions beneath Floreana (i.e. where H_2O and La act as incompatible trace components).

To distinguish between these two different possibilities, we can consider the trace element and isotopic composition of the Floreana basalts (including the enriched samples with estimated H_2O concentrations >0.8 wt%). Notably, there is greater heterogeneity in the trace element and isotopic composition of the Floreana basalts than at any other location in the Galápagos Archipelago, indicating the presence of a heterogeneous mantle source beneath the island (Harpp et al., 2014). Importantly, any differences in the lithological properties and/or volatile content of the mantle components involved in the genesis of the Floreana lavas will cause offsets in their solidus temperatures and melt productivities. Therefore, variations in the mean melt fraction of the Floreana mantle source is expected to drive changes in the isotopic composition of the resulting basalts (by influencing the relative contribution of melts from the different, isotopically distinct, mantle components) as well as incompatible trace element ratios such as $[La/Sm]_n$ (where *n* indicates normalisation to the primitive mantle composition of Sun and McDonough, 1989). In fact, when we consider the available isotope and trace element data from the Floreana basalts with estimated H_2O concentrations <0.8 wt%, we find that a statistically significant correlation exists between $[La/Sm]_n$ and $^{206}Pb/^{204}Pb$ (Fig. 9). This correlation, however, does not extend to the highly enriched Floreana basalts (i.e., those that have estimated H_2O contents >0.8 wt%), which are isotopically indistinguishable from the rest of the Floreana lavas. We therefore suggest that their anomalous trace element signature is a consequence of crustal processing in magmatic mush zones, rather than variations in the extent of mantle melting (Fig. 9; Gleeson et al., 2020a; Harpp et al., 2014; Lyons et al., 2007).

In addition, there is substantial geochemical and textural evidence preserved in the Floreana xenoliths to support the interpretation that reactive porous flow is an important geochemical process in mush zones beneath the island. For example, trace element enrichment in the wehrlite xenoliths cannot be explained through simple fractional crystallisation, but can be explained by models that account for melt-mush reaction during reactive porous flow (Gleeson et al., 2020a). Additionally, the enrichment in the trace element composition of the cumulate clinopyroxenes are

commonly more extreme at the crystal rims compared to their cores, consistent with trace element enrichment originating through magma processing in a mush rather than initial crystallisation from anomalously enriched mantle melts (Gleeson et al. 2020a). Finally, all clinopyroxene crystals that have anomalously high equilibrium-melt H_2O contents also have incompatible trace element signatures that are too enriched to be in equilibrium with the majority of the erupted Floreana basalts (Gleeson et al., 2020a), and, as a result, we favour the reactive porous flow hypothesis presented above.

In summary, the kernel density distributions calculated for the melt H_2O contents in equilibrium with the Floreana NAMs and the predicted melt H_2O concentrations calculated via whole-rock trace element data (i.e. La concentrations) have primary peaks at ~0.4–0.8 wt% H_2O. This represents the typical H_2O concentration of Floreana sub-volcanic melts which have not been modified by cumulate processes. However, reactive porous flow in highly crystalline magma storage regions generates local incompatible trace element-enrichment (Gleeson et al. 2020a), resulting in melts with H_2O concentrations >>0.8 wt%. Rare, trace element enriched, whole-rock samples from Floreana (with estimated H_2O concentrations >0.8 wt%) likely contain a substantial contribution of melts which have undergone geochemical enrichment by reactive porous flow, and indicate that melts in highly crystalline sub-volcanic storage regions are occasionally remobilised and erupted.

5.2 Volatile systematics in the western Galápagos Archipelago

While our new data represents the first systematic constraints on the volatile contents of the Floreana magmas in the south-eastern Galápagos, published volatile data provides insights into the volatile systematics of the western Galápagos volcanic systems. For example, Peterson et al. (2017) report the volatile content (H_2O, F, Cl, S, and CO_2) of submarine glasses collected from a series of dredging expeditions across the Galápagos Platform. Included within their dataset is a suite of submarine basalts from the western margin of Fernandina, at the leading edge of the Galápagos mantle plume (Fig. 1). These basalts have high $^3He/^4He$ ratios that are characteristic of Fernandina

magmas (Harpp and White, 2001; Peterson et al. 2017). In addition, olivine-hosted melt inclusions from a nearby submarine lava flow on the western margin of Fernandina have also been analysed for their volatile contents (Fig. 1). Together, these submarine glass and melt inclusion analyses provide important insights into the volatile systematics of the Fernandina magmatic system and, by comparing our new Floreana data with these published volatile records, allow us to investigate the magmatic volatile contents in two regions of the archipelago with highly contrasting magmatic storage conditions and eruptive styles (Gleeson et al., 2020a; Harpp and Geist, 2018; Stock et al., 2020).

The Fernandina melt inclusions show a positive correlation between Cl and incompatible trace element concentrations (e.g. Nb, K; Fig. 10; Koleszar et al., 2009), with Cl/K ratios of 0.038 ±0.016, consistent with the similar compatibilities of these elements during mantle melting (Lassiter et al., 2002). In contrast, matrix glasses in the Fernandina submarine lavas have a narrow range of K and Nb concentrations, but a relatively large range of Cl concentrations (~150–450 ppm Cl) and thus variable Cl/K ratios (Fig. 10; Peterson et al., 2017). This variability in the Cl/K ratio of the Fernandina submarine glasses likely reflects assimilation of a Cl-rich component, such as a hydrothermal brine (Jackson et al., 2015; Kendrick et al., 2015). Additionally, the correlation between Cl concentrations and H_2O/La ratios in the Fernandina submarine matrix glasses (r^2=0.723), indicates that brine assimilation has also impacted on their H_2O concentrations (Fig. 10).

By considering volatile and non-volatile trace element systematics in the Fernandina matrix glasses, it is possible to calculate the extent of Cl and H_2O assimilation (Kendrick et al., 2015). First, the amount of Cl that was assimilated by each sample can be estimated by calculating the amount of Cl required to match the Cl/K ratio of the Fernandina melt inclusions (0.038) and subtracting this from the measured Cl concentration. The amount of assimilated H_2O can then be calculated if the H_2O/Cl ratio of the assimilated component can be determined, which is achieved by taking the intercept of a linear regression through the glass data on plots of H_2O/Cl vs K/Cl or F/Cl (Kendrick et al., 2015). The

Fernandina submarine matrix glasses of Peterson et al. (2017) show a linear correlation between H_2O/Cl and K/Cl, which indicates that the assimilated brine component has a H_2O/Cl ratio of ~17.1 (Fig. 10). Therefore, using the calculated amount of Cl assimilated by each sample, and the H_2O/Cl ratio of the assimilated component, it is possible to calculate the amount of H_2O that has been assimilated.

The kernel density distribution of the uncorrected Fernandina matrix glass H_2O/La ratio is centred at ~500, with a long tail extending to higher values (>800; Fig. 10). However, using the method above, we can correct the H_2O content of the Fernandina submarine glasses to account for the influence of brine assimilation. After correction, the data forms a Gaussian distribution with a mean H_2O/La ratio of 410, spread over a narrow range of values (2σ = 83; Fig. 10). These corrected data give the H_2O/La ratios of the Fernandina primary melts, with the narrow range reflecting their limited H_2O/La variability, consistent with the elemental and isotopic homogeneity of Fernandina erupted basalts (Geist et al., 2014; Harpp and Geist, 2018).

The H_2O content of olivine-hosted melt inclusions from Fernandina are also influenced by secondary processes (Koleszar et al., 2009), as indicated by their constant H_2O contents (0.8 – 1.0 wt%) and H_2O/La ratios that extend to high values (>800; Fig. 10). The high H_2O/La ratios of some of the Fernandina melt inclusions can be explained by diffusive hydration of primitive melt inclusions (with low initial concentrations of H_2O) as their host olivine crystals are entrained into a more evolved (and thus H_2O-rich) magma prior to eruption. As H^+ diffuses significantly faster than La through the olivine crystal lattice, the H_2O concentration of the olivine-hosted melt inclusions will re-equilibrate with the external H_2O-rich melt (~0.8 - 1 wt% H_2O) on timescales of hours-to-days (Fig. 10; Gaetani et al., 2012). In contrast, the melt inclusion La concentrations will remain constant over long timescales (as diffusion of La is several orders of magnitude slower than that of H_2O through silicate melts and olivine host crystals; Zhang et al., 2010; Zhang and Ni, 2010), resulting in high H_2O/La ratios (Hartley et al., 2015).

Using the H_2O/La ratio of the Fernandina submarine glasses, corrected for brine assimilation, we can estimate the H_2O contents of the Fernandina melt inclusions at the time of entrapment (by taking the PEC corrected La concentrations of Koleszar et al., 2009). The predicted H_2O concentrations vary from ~0.1 to 0.62 wt%, with the most primitive melt inclusions showing the greatest variability in H_2O contents. More evolved (lower Mg#) melt inclusions typically have a more restricted range of H_2O concentrations and the mean H_2O concentrations increase with decreasing Mg# and olivine Fo content, consistent with H_2O behaving as an incompatible element during concurrent mixing and crystallisation (Fig. 8). The brine-corrected H_2O contents of the Fernandina submarine glasses plot along the same fractional crystallisation trajectory as the mean composition of the melt inclusions. As a result, the Fernandina melt inclusion and submarine glass data indicate that the Fernandina magmas are controlled by concurrent mixing and crystallisation of mantle-derived melts (Koleszar et al., 2009; Maclennan, 2008).

Furthermore, as gabbroic xenoliths from Floreana are hypothesised to sample an ancient magmatic system, i.e. from when the island was located close to the Galápagos plume stem (Lyons et al., 2007), we would expect our new clinopyroxene volatile data from these nodules to match the volatile contents of erupted products from present-day plume-proximal volcanoes in the western archipelago. In fact, the calculated equilibrium melt H_2O contents from one of our gabbroic xenoliths (17MMSG04b; 0.64 ±0.12 wt%) does overlap with the brine-corrected H_2O concentrations in the submarine glasses from the western archipelago (Peterson et al., 2017), but those in our other gabbroic sample (17MMSG03b; 1.19 ±0.13 wt%) are significantly higher than typical melt H_2O analyses from the western Galápagos Archipelago. The clinopyroxene H_2O contents of these two gabbroic xenoliths are unlikely to be related to each other by simple fractional crystallisation as the clinopyroxene crystals from both xenoliths have similar major element signatures (e.g., Mg#; Gleeson et al. 2020a). Instead, the high H_2O concentrations observed in clinopyroxene crystals from sample 17MMSG03b might record geochemical enrichment by the same reactive porous flow process that has been identified in cumulate mush zones beneath Floreana (Gleeson et al., 2020a),

but more data is required to confirm this hypothesis. As a result, the high H_2O concentrations measured in gabbro 17MMSG03b could indicate that reactive porous flow operates beneath present-day volcanoes in the western archipelago, but is yet to be identified in erupted products (signatures of reactive porous flow in erupted magmas may include an over-enrichment in incompatible trace elements with increasing differentiation; Lissenberg and MacLeod, 2016); the ancient Floreana magmatic system was distinct from the magmatic systems currently underlying the plume-proximal western volcanoes (Harpp and Geist, 2018); or that the H_2O content of the gabbroic xenoliths is reset by interaction with more recent Floreana magmas.

5.3 Contrasting Fernandina and Floreana basalt H_2O concentrations

Our new data from the Floreana basalts and xenoliths, and re-evaluation of published data from Fernandina, indicate that these volcanoes have distinct volatile histories: the H_2O contents of the Fernandina basalts are primarily controlled by fractional crystallisation and magma mixing, whereas some Floreana basalts are influenced by H_2O-rich magmas generated by reactive porous flow within crystal-rich sub-volcanic mush zones. To directly compare the volatile contents of magmas from these locations, we reconstruct initial melt inclusion and whole-rock H_2O concentrations (i.e. prior to alteration by secondary processes) using their measured La concentrations and the characteristic H_2O/La ratio of each magmatic system as determined above.

Comparing reconstructed initial melt inclusion and whole-rock H_2O concentrations indicates that the Floreana magmas typically have slightly higher H_2O contents than the Fernandina magmas at an equivalent melt Mg# (Fig. 8). For example, at Mg# ~0.65, Floreana magmas contain ~0.4–0.8 wt% H_2O (0.6 wt% average), whereas Fernandina magmas contain 0.1–0.67 wt% H_2O (0.4 wt% average; Fig. 8; Koleszar et al., 2009; Peterson et al., 2017). Harpp et al. (2014) hypothesised that the abundance of explosive volcanism on Floreana might be due to high magmatic H_2O contents. However, we suggest that the difference in magmatic H_2O concentrations at Floreana and Fernandina is too small to account for their different eruptive styles, especially as Fernandina

magmas typically erupt at lower MgO concentrations when they have very similar H_2O contents to the more mafic erupted melts on Floreana.

6 INSIGHTS INTO THE VOLATILE CONTENT OF THE GALÁPAGOS MANTLE SOURCE

6.1 THE H_2O SYSTEMATICS OF THE GALÁPAGOS MANTLE PLUME

Radiogenic isotope, trace element, and major element data indicate that the Galápagos mantle plume is heterogeneous over a variety of length-scales (Gibson et al., 2012; Gleeson et al., 2021; Harpp and White, 2001). In fact, the mantle sources of the Floreana and Fernandina basalts likely contain at least 2 distinct components that may have different volatile contents or lithological properties and may thus be characterised by different solidus temperatures and melt productivities (Harpp et al., 2014; Katz et al., 2003; Lambart et al., 2016). Therefore, to determine the contribution of each source component to the trace element budget of the Fernandina and Floreana basalts, and by extension constrain the source volatile contents, we require knowledge of the source trace element compositions, source proportions and melting behaviours (e.g. Rudge et al., 2013). However, accurate constraints on the trace element composition of the mantle source components, and their relative proportions in the Galápagos mantle plume, are not currently available.

For example, the Fernandina basalts have unradiogenic He isotope ratios ($^3He/^4He$ ~30 R/R_A), which has been used to suggest that a primordial or primitive mantle component is present in the mantle source region of the Fernandina basalts (Kurz et al., 2009). In fact, previous studies have estimated the H_2O content of the Fernandina mantle source through the combination of measured H_2O/Ce ratios and published estimates for the trace element composition of the primitive mantle (Peterson et al., 2017). Yet, both the trace element systematics (e.g. the high TITAN signature; that is, high primitive mantle normalised concentrations of Ti, Ta, and Nb relative to elements with similar compatibilities during mantle melting) and radiogenic isotope composition of the Fernandina basalts

do not match those expected from melting of a primitive mantle component (Farley et al., 1992; Harpp and Weis, 2020; Harpp and White, 2001; Jackson et al., 2008). As a result, there is substantial evidence to suggest that a primitive mantle trace element composition is not appropriate for the Fernandina source and could lead to significant errors in the estimated source H_2O concentrations if used in this manner. Moreover, He might be decoupled from lithophile elements such as Sr or La during mantle melting (Graham et al., 2014), further demonstrating that high $^{3}He/^{4}He$ ratios alone cannot be used to justify the use of a primitive mantle trace element estimate for the Fernandina mantle source.

No robust estimates exist for the trace element composition of the Floreana mantle source. Recent work has shown that the radiogenic Pb isotope composition of the Floreana basalts in the south-eastern Galápagos is similar to that of the global HIMU mantle (Chauvel et al., 1992; Harpp et al., 2014; Weiss et al., 2016) and an estimate for the trace element composition of the HIMU mantle was proposed by Weiss et al. (2016). However, there are several key differences between the Floreana basalts and typical HIMU basalts that indicate that the Weiss et al. (2016) estimate for the trace element composition of the HIMU mantle is unlikely to be appropriate for the Floreana mantle source. For example, the Floreana basalts contain more radiogenic $^{87}Sr/^{86}Sr$ signatures than typical HIMU basalts (Harpp and White, 2001) and the high Pb concentration of most Floreana lavas, and therefore their low Ce/Pb ratios, are inconsistent with the signatures expected for true HIMU basalts (Harpp et al., 2014). As a result, using published estimates for the trace element composition of the primitive mantle and HIMU source to determine the H_2O content of the Fernandina and Floreana mantle source regions, respectively, is not appropriate.

More work is required to accurately determine the trace element composition of the various mantle components in the Galápagos plume. One promising method that may provide future insights into the composition of the Galápagos plume is the integration of multi-component mantle melting models with Markov Chain Monte Carlo algorithms (e.g. Brown et al., 2020; Gleeson et al., 2020b).

Nevertheless, in the absence of accurate source trace element estimates, we can consider the H_2O/REE systematics of the Galápagos basalts to determine the relative 'hydration' of the different Galápagos source components with respect to their trace element composition. Specifically, we can use our new data, alongside published volatile analyses from basalts across the archipelago and nearby spreading centre (Cushman et al., 2004; Gleeson and Gibson, 2021; Ingle et al., 2010; Koleszar et al., 2009; Peterson et al., 2017), to investigate how the H_2O/REE systematics of the Galápagos basalts are related to the extent of geochemical enrichment.

The H_2O/La systematics of the depleted peridotite component in the Galápagos mantle plume (the Depleted Galápagos Mantle; DGM) has recently been determined through analysis of plume-influenced MORBs along the Galápagos Spreading Centre (GSC; Gleeson and Gibson, 2021). This data revealed that isotopically depleted basalts associated with the Galápagos plume (that have not been influenced by assimilation of Cl-rich brine components) have H_2O/La ratios of ~750. In contrast, trace element and isotopically enriched basalts from the GSC (i.e. with $[La/Sm]_n>2$) exhibit H_2O/La ratios of 350 – 400, similar to the H_2O/La ratios observed in the Fernandina and Floreana basalts (410 ±82 and 270 – 370, respectively; Fig. 11).

Overall, these data indicate that the H_2O/La ratio of the enriched mantle components in the Galápagos plume are lower than that of the DGM. This 'dehydration' signature indicates that the H_2O^{enr}/H_2O^{DGM} ratio of the Galápagos mantle plume (i.e. the concentration of H_2O in the enriched source components relative to the DGM) is smaller than La^{enr}/La^{DGM}. Notably, the 'dehydration' signature is also observed when we consider the H_2O/Ce ratio of the enriched Galápagos basalts instead of H_2O/La. In particular, the H_2O/Ce ratio of basalts from Fernandina and Floreana are <200 (based on our analysis above), whereas depleted plume-influenced GSC basalts have H_2O/Ce ratios between 200 and 250 (Fig. 11; Gleeson and Gibson, 2021).

The origin of these differences in the H_2O/REE systematics of the Galápagos plume basalts is uncertain, but it is notable that this is not the only region globally where such variations have been

observed. In fact, similar or even larger variations are observed in the H_2O/La and H_2O/Ce ratio of MORBs and OIBs worldwide. For example, MORBs erupted north of Iceland along the Mid-Atlantic Ridge have H_2O/Ce ratios of 280 ±37 (Michael, 1995), whereas EM-type basalts erupted in the northern Pacific (between 0°N and 20°N along the East Pacific Rise) have H_2O/Ce ratios of only 110 ±20 (Dixon et al., 2017). The origin of these variations in the H_2O/REE systematics of MORBs and OIBs remains debated, but both dehydration of the slab during subduction and diffusive loss of H_2O from enriched components in the mantle may play an important role in the formation of enriched mantle components with relatively low H_2O/La and H_2O/Ce systematics (Cabral et al., 2014; Dixon et al., 2017).

6.2 Halogen-rich nature of the Floreana mantle source

As our new data from the Floreana melt inclusions and melt embayments reveals correlations between Cl and highly incompatible trace elements (e.g. Ba, K) and no significant correlation between the halogens (F and Cl) and H_2O or S (at the 95% significance level), the measured concentrations of F and Cl in the Floreana glasses are unlikely to be influenced by secondary processes such as degassing or brine assimilation (Fig. 6). Therefore, the F/Nd and Cl/K ratios measured in the Floreana melt inclusions and embayments (35.1 ±5.1 and 0.096 ±0.030, respectively) can be used to qualitatively evaluate the F and Cl content of the FLO mantle source (assuming that these ratios are unfractionated during mantle melting). Notably, our measured Floreana melt F/Nd and Cl/K ratios are substantially higher and more variable than in erupted basalts from Fernandina in the western Galápagos (F/Nd ~20.2, Cl/K ~0.038; Koleszar et al., 2009; Peterson et al., 2017; Fig. 7) and plume influenced basalts from the GSC (Gleeson and Gibson, 2021).

The high $^{206}Pb/^{204}Pb$ mantle source beneath Floreana (i.e., the FLO mantle; Harpp and Weis, 2020; Harpp and White, 2001), therefore, appears to be unique in the Galápagos, not only for its isotopic composition but also its halogen content. In addition, if we assume that contribution of melts from other mantle source components to the Floreana basalts will lead to a decrease in the F/Nd and Cl/K

ratios of the Floreana basalts, we can take the highest values measured in our melt inclusions and embayments to place constraints on the minimum F/Nd and Cl/K ratios of the Galápagos FLO mantle (47.5 and 0.124, respectively).

Comparison of our new Floreana data with other global OIBs reveals that such high F/Nd and Cl/K ratios are very rare (Kendrick et al., 2014; Métrich et al., 2014; Sides et al., 2014; Workman et al., 2006; Fig. 7). In fact, comparable F/Nd and Cl/K values have only been identified at localities that are dominated by melting of a HIMU mantle source (e.g. Mangaia and Tubuai; Cabral et al., 2014; Hanyu et al., 2019). Therefore, our new data suggests that true HIMU localities are not the only regions in the Earth's mantle that can contain high concentrations of F and Cl, and indicates that the FLO mantle source might be an important reservoir of halogens in the Galápagos mantle plume (despite its relatively localised influence).

7 CONCLUSIONS

By integrating volcanic glass and NAM analyses from different parts of the Galápagos Archipelago, we gain new insights into the behaviour and mantle source contents of volatiles across a single OIB system. The H_2O contents of submarine glasses (corrected for brine assimilation) and melt inclusions from Fernandina indicate that magma volatile contents in the western Galápagos Archipelago are primarily controlled by concurrent mixing and crystallisation of heterogeneous mantle melts. In contrast, our new data from Floreana reveal that magma volatile contents in the south-eastern Galápagos Archipelago are affected by reactive porous flow through crystal-rich mush zones. Despite these different processes controlling volatile behaviour during magmatic evolution, the pre-eruptive H_2O contents of Floreana and Fernandina magmas are likely very similar (~0.4–0.9 wt%), suggesting that differences in the style of volcanic activity on the two islands are not driven by differences in their volatile contents.

Calculating the volatile contents of mantle source components contributing to erupted basalts on Floreana and Fernandina is inhibited by uncertainties in their trace element compositions and relative proportions. Nevertheless, our new data indicates that the enriched mantle components in the Galápagos plume are characterised by lower H_2O/La ratios than the DGM, and a relative dehydration of these enriched components with respect to their trace element compositions. Furthermore, our data reveals that the Floreana basalts have high F/Nd and Cl/K ratios, are 2-3 time greater than those measured in other parts of the Galápagos Archipelago and may indicate that the FLO mantle source represents an important reservoir of halogens in the Galápagos plume.

CODE AVAILABILTY

Add code developed for this study are available via
https://github.com/gleesonm1/MagmaDecompress

ACKNOWLEDGEMENTS

This study was supported by a NERC (Natural Environmental Research Council) Research Training Student Grant (NE/L002507/1) awarded to M.L.M.G, as well as grant from the Darwin Galápagos Fund awarded to S.A.G. M. J. S. was supported by a Charles Darwin and Galápagos Islands Junior Research Fellowship at Christ's College, Cambridge. SIMS analysis was made possible by the NERC IMF grant IMF622/0517. We are grateful to Iris Buisman for help with EPMA analysis and SEM images. We thank Margaret Hartley for comments on an early version of this manuscript and are grateful for the support of the Charles Darwin Research Station and the Galápagos National Park authorities for their assistance with fieldwork. Antonio Proaño, Lenin Cruz and the crew of the Pirata provided invaluable help in the field.

REFERENCES

Adam, J., Turner, M., Hauri, E.H., Turner, S., 2016. Crystal/melt partitioning of water and other volatiles during the near-solidus melting of mantle peridotite: Comparisons with non-volatile incompatible elements and implications for the generation of intraplate magmatism. Am. Mineral. 101, 876–888. https://doi.org/10.2138/am-2016-5437

Allan, J.F., Simkin, T., 2000. Fernandina Volcano's evolved, well-mixed basalts: Mineralogical and petrological constraints on the nature of the Galapagos plume. J. Geophys. Res. Solid Earth 105, 6017–6041. https://doi.org/10.1029/1999JB900417

Asimow, P.D., Dixon, J.E., Langmuir, C.H., 2004. A hydrous melting and fractionation model for mid-ocean ridge basalts: Application to the Mid-Atlantic Ridge near the Azores. Geochem. Geophys. Geosystems 5, n/a-n/a. https://doi.org/10.1029/2003GC000568

848 Asimow, P.D., Langmuir, C.H., 2003. The importance of water to oceanic mantle melting regimes.
849 Nature 421, 815–820. https://doi.org/10.1038/nature01429
850 Barth, A., Newcombe, M., Plank, T., Gonnermann, H., Hajimirza, S., Soto, G.J., Saballos, A., Hauri, E.,
851 2019. Magma decompression rate correlates with explosivity at basaltic volcanoes —
852 Constraints from water diffusion in olivine. J. Volcanol. Geotherm. Res. 387, 106664.
853 https://doi.org/10.1016/j.jvolgeores.2019.106664
854 Bow, C.S., Geist, D.J., 1992. Geology and petrology of Floreana Island, Galapagos Archipelago,
855 Ecuador. J. Volcanol. Geotherm. Res. 52, 83–105. https://doi.org/10.1016/0377-
856 0273(92)90134-Y
857 Brown, E.L., Petersen, K.D., Lesher, C.E., 2020. Markov chain Monte Carlo inversion of mantle
858 temperature and source composition, with application to Reykjanes Peninsula, Iceland.
859 Earth Planet. Sci. Lett. 532, 116007. https://doi.org/10.1016/j.epsl.2019.116007
860 Cabral, R.A., Jackson, M.G., Koga, K.T., Rose-Koga, E.F., Hauri, E.H., Whitehouse, M.J., Price, A.A.,
861 Day, J.M.D., Shimizu, N., Kelley, K.A., 2014. Volatile cycling of H_2O, CO_2, F, and Cl in the
862 HIMU mantle: A new window provided by melt inclusions from oceanic hot spot lavas at
863 Mangaia, Cook Islands. Geochem. Geophys. Geosystems 15, 4445–4467.
864 https://doi.org/10.1002/2014GC005473
865 Chadwick, W.W., Jónsson, S., Geist, D.J., Poland, M., Johnson, D.J., Batt, S., Harpp, K.S., Ruiz, A.,
866 2011. The May 2005 eruption of Fernandina volcano, Galápagos: The first circumferential
867 dike intrusion observed by GPS and InSAR. Bull. Volcanol. 73, 679–697.
868 https://doi.org/10.1007/s00445-010-0433-0
869 Chauvel, C., Hofmann, A.W., Vidal, P., 1992. himu-em: The French Polynesian connection. Earth
870 Planet. Sci. Lett. 110, 99–119. https://doi.org/10.1016/0012-821X(92)90042-T
871 Costa, F., Shea, T., Ubide, T., 2020. Diffusion chronometry and the timescales of magmatic processes.
872 Nat. Rev. Earth Environ. https://doi.org/10.1038/s43017-020-0038-x
873 Cushman, B., Sinton, J., Ito, G., Eaby Dixon, J., 2004. Glass compositions, plume-ridge interaction, and
874 hydrous melting along the Galápagos Spreading Center, 90.5°W to 98°W. Geochem.
875 Geophys. Geosystems 5. https://doi.org/10.1029/2004GC000709
876 Dalou, C., Koga, K. T., Shimizu, N., 2012. Experimental determination of F and Cl partitioning
877 between lherzolite and basaltic melt. Contrib. Mineral. Petrol. 163, 591–609.
878 Danyushevsky, L.V., Plechov, P., 2011. Petrolog3: Integrated software for modeling crystallization
879 processes. Geochem. Geophys. Geosystems 12, n/a-n/a.
880 https://doi.org/10.1029/2011GC003516
881 deGraffenried, R.L., Shea, T., 2021. Using Volatile Element Concentration Profiles in Crystal-Hosted
882 Melt Embayments to Estimate Magma Decompression Rate: Assumptions and Inherited
883 Errors. Geochem. Geophys. Geosystems 22. https://doi.org/10.1029/2021GC009672
884 Dixon, J.E., 1997. Degassing of alkalic basalts. Am. Mineral. 82, 368–378.
885 https://doi.org/10.2138/am-1997-3-415
886 Dixon, J.E., Bindeman, I.N., Kingsley, R.H., Simons, K.K., Le Roux, P.J., Hajewski, T.R., Swart, P.,
887 Langmuir, C.H., Ryan, J.G., Walowski, K.J., Wada, I., Wallace, P.J., 2017. Light Stable Isotopic
888 Compositions of Enriched Mantle Sources: Resolving the Dehydration Paradox. Geochem.
889 Geophys. Geosystems 18, 3801–3839. https://doi.org/10.1002/2016GC006743
890 Edmonds, M., Kohn, S.C., Hauri, E.H., Humphreys, M.C.S., Cassidy, M., 2016. Extensive, water-rich
891 magma reservoir beneath southern Montserrat. Lithos 252–253, 216–233.
892 https://doi.org/10.1016/j.lithos.2016.02.026
893 Farley, K.A., Natland, J.H., Craig, H., 1992. Binary mixing of enriched and undegassed (primitive?)
894 mantle components (He, Sr, Nd, Pb) in Samoan lavas. Earth Planet. Sci. Lett. 111, 183–199.
895 https://doi.org/10.1016/0012-821X(92)90178-X
896 Ferguson, D.J., Gonnermann, H.M., Ruprecht, P., Plank, T., Hauri, E.H., Houghton, B.F., Swanson,
897 D.A., 2016. Magma decompression rates during explosive eruptions of Kīlauea volcano,

898 Hawaii, recorded by melt embayments. Bull. Volcanol. 78, 71.
899 https://doi.org/10.1007/s00445-016-1064-x
900 Ferriss, E., Plank, T., Walker, D., 2016. Site-specific hydrogen diffusion rates during clinopyroxene
901 dehydration. Contrib. Mineral. Petrol. 171, 55. https://doi.org/10.1007/s00410-016-1262-8
902 Friedman, I., Long, W., 1976. Hydration Rate of Obsidian. Science 191, 347–352.
903 https://doi.org/10.1126/science.191.4225.347
904 Gaetani, G.A., Grove, T.L., 1998. The influence of water on melting of mantle peridotite. Contrib.
905 Mineral. Petrol. 131, 323–346. https://doi.org/10.1007/s004100050396
906 Gaetani, G.A., O'Leary, J.A., Shimizu, N., Bucholz, C.E., Newville, M., 2012. Rapid reequilibration of
907 H2O and oxygen fugacity in olivine-hosted melt inclusions. Geology 40, 915–918.
908 https://doi.org/10.1130/G32992.1
909 Geist, D.J., Bergantz, G., Chadwick, W.W., 2014. Galápagos Magma Chambers, in: Harpp, K.S.,
910 Mittelstaedt, E., d'Ozouville, N., Graham, D.W. (Eds.), Geophysical Monograph Series. John
911 Wiley & Sons, Inc, Hoboken, New Jersey, pp. 55–69.
912 https://doi.org/10.1002/9781118852538.ch5
913 Geist, D.J., Fornari, D.J., Kurz, M.D., Harpp, K.S., Adam Soule, S., Perfit, M.R., Koleszar, A.M., 2006.
914 Submarine Fernandina: Magmatism at the leading edge of the Galápagos hot spot.
915 Geochem. Geophys. Geosystems 7, n/a-n/a. https://doi.org/10.1029/2006GC001290
916 Geist, D.J., White, W.M., McBirney, A.R., 1988. Plume-asthenosphere mixing beneath the Galapagos
917 archipelago. Nature 333, 657–660. https://doi.org/10.1038/333657a0
918 Ghiorso, M.S., Gualda, G.A.R., 2015. An H2O–CO2 mixed fluid saturation model compatible with
919 rhyolite-MELTS. Contrib. Mineral. Petrol. 169, 53. https://doi.org/10.1007/s00410-015-1141-
920 8
921 Gibson, S.A., Geist, D.G., Day, J.A., Dale, C.W., 2012. Short wavelength heterogeneity in the
922 Galápagos plume: Evidence from compositionally diverse basalts on Isla Santiago. Geochem.
923 Geophys. Geosystems 13. https://doi.org/10.1029/2012GC004244
924 Gibson, S.A., Richards, M.A., 2018. Delivery of deep-sourced, volatile-rich plume material to the
925 global ridge system. Earth Planet. Sci. Lett. 499, 205–218.
926 https://doi.org/10.1016/j.epsl.2018.07.028
927 Gleeson, M., Gibson, S., 2021. Insights into the nature of plume-ridge interaction and outflux of H2O
928 from the Galápagos Spreading Centre. *Geochemistry, Geophysics, Geosystems.*
929 e2020GC009560. https://doi.org/10.1029/2020GC009560
930 Gleeson, M., Soderman, C., Matthews, S., Cottaar, S. and Gibson, S., 2021. Geochemical constraints
931 on the structure of the Earth's deep mantle and the origin of the LLSVPs. *Geochemistry,*
932 *Geophysics, Geosystems*, e2021GC009932. https://doi.org/10.1029/2021GC009932
933 Gleeson, M.L.M., Gibson, S.A., 2019. Crustal controls on apparent mantle pyroxenite signals in
934 ocean-island basalts. Geology. https://doi.org/10.1130/G45759.1
935 Gleeson, Matthew L M, Gibson, S.A., Stock, M.J., 2020a. Upper mantle mush zones beneath low melt
936 flux ocean island volcanoes: insights from Isla Floreana, Galápagos. J. Petrol. egaa094.
937 https://doi.org/10.1093/petrology/egaa094
938 Gleeson, Matthew L.M., Gibson, S.A., Williams, H.M., 2020b. Novel insights from Fe-isotopes into the
939 lithological heterogeneity of Ocean Island Basalts and plume-influenced MORBs. Earth
940 Planet. Sci. Lett. 535, 116114. https://doi.org/10.1016/j.epsl.2020.116114
941 Graham, D.W., Hanan, B.B., Lupton, J.E., Hoernle, K., Werner, R., Christie, D.M., Sinton, J.M., 2014.
942 Helium Isotope Variations and Mantle Plume-Spreading Ridge Interactions Along the
943 Galápagos Spreading Center, in: Harpp, K.S., Mittelstaedt, E., d'Ozouville, N., Graham, D.W.
944 (Eds.), Geophysical Monograph Series. John Wiley & Sons, Inc, Hoboken, New Jersey, pp.
945 393–414. https://doi.org/10.1002/9781118852538.ch18
946 Hanyu, T., Shimizu, K., Ushikubo, T., Kimura, J.-I., Chang, Q., Hamada, M., Ito, M., Iwamori, H.,
947 Ishikawa, T., 2019. Tiny droplets of ocean island basalts unveil Earth's deep chlorine cycle.
948 Nat. Commun. 10. https://doi.org/10.1038/s41467-018-07955-8

949 Harpp, K.S., Geist, D.J., 2018. The Evolution of Galápagos Volcanoes: An Alternative Perspective.
950 Front. Earth Sci. 6. https://doi.org/10.3389/feart.2018.00050
951 Harpp, K.S., Geist, D.J., Koleszar, A.M., Christensen, B., Lyons, J., Sabga, M., Rollins, N., 2014. The
952 Geology and Geochemistry of Isla Floreana, Galápagos: A Different Type of Late-Stage Ocean
953 Island Volcanism, in: Harpp, K.S., Mittelstaedt, E., d'Ozouville, N., Graham, D.W. (Eds.),
954 Geophysical Monograph Series. John Wiley & Sons, Inc, Hoboken, New Jersey, pp. 71–117.
955 https://doi.org/10.1002/9781118852538.ch6
956 Harpp, K.S., Weis, D., 2020. Insights Into the Origins and Compositions of Mantle Plumes: A
957 Comparison of Galápagos and Hawai'i. Geochem. Geophys. Geosystems 21.
958 https://doi.org/10.1029/2019GC008887
959 Harpp, K.S., White, W.M., 2001. Tracing a mantle plume: Isotopic and trace element variations of
960 Galápagos seamounts. Geochem. Geophys. Geosystems 2, n/a-n/a.
961 https://doi.org/10.1029/2000GC000137
962 Hartley, M.E., Neave, D.A., Maclennan, J., Edmonds, M., Thordarson, T., 2015. Diffusive over-
963 hydration of olivine-hosted melt inclusions. Earth Planet. Sci. Lett. 425, 168–178.
964 https://doi.org/10.1016/j.epsl.2015.06.008
965 Hauri, E., Gaetani, G., Green, T., 2006. Partitioning of water during melting of the Earth's upper
966 mantle at H2O-undersaturated conditions. Earth Planet. Sci. Lett. 248, 715–734.
967 https://doi.org/10.1016/j.epsl.2006.06.014
968 Hirth, G., Kohlstedt, D., 2003. Rheology of the upper mantle and the mantle wedge: A view from the
969 experimentalists, in: Eiler, J. (Ed.), Geophysical Monograph Series. American Geophysical
970 Union, Washington, D. C., pp. 83–105. https://doi.org/10.1029/138GM06
971 Hirth, G., Kohlstedt, D.L., 1996. Water in the oceanic upper mantle: implications for rheology, melt
972 extraction and the evolution of the lithosphere. Earth Planet. Sci. Lett. 144, 93–108.
973 https://doi.org/10.1016/0012-821X(96)00154-9
974 Hoernle, K., Werner, R., Morgan, J.P., Garbe-Schönberg, D., Bryce, J., Mrazek, J., 2000. Existence of
975 complex spatial zonation in the Galápagos plume. Geology 28, 435.
976 https://doi.org/10.1130/0091-7613(2000)28<435:EOCSZI>2.0.CO;2
977 Hofmann, A.W., 1997. Mantle geochemistry: the message from oceanic volcanism. Nature 385, 219–
978 229. https://doi.org/10.1038/385219a0
979 Hooft, E.E.E., Toomey, D.R., Solomon, S.C., 2003. Anomalously thin transition zone beneath the
980 Galápagos hotspot. Earth Planet. Sci. Lett. 216, 55–64. https://doi.org/10.1016/S0012-
981 821X(03)00517-X
982 Humphreys, M.C.S., Kearns, S.L., Blundy, J.D., 2006. SIMS investigation of electron-beam damage to
983 hydrous, rhyolitic glasses: Implications for melt inclusion analysis. Am. Mineral. 91, 667–679.
984 https://doi.org/10.2138/am.2006.1936
985 Iacono-Marziano, G., Morizet, Y., Le Trong, E., Gaillard, F., 2012. New experimental data and semi-
986 empirical parameterization of H2O–CO2 solubility in mafic melts. Geochim. Cosmochim. Acta
987 97, 1–23. https://doi.org/10.1016/j.gca.2012.08.035
988 Iacovino, K., Matthews, S., Wieser, P., Moore, G., Bégué, F., 2020. VESIcal Part I: An open-source
989 thermodynamic model engine for mixed volatile (H2O-CO2) solubility in silicate melts
990 (preprint). Earth Sciences. https://doi.org/10.31223/X5D606
991 Ingle, S., Ito, G., Mahoney, J.J., Chazey, W., Sinton, J., Rotella, M., Christie, D.M., 2010. Mechanisms
992 of geochemical and geophysical variations along the western Galápagos Spreading Center.
993 Geochem. Geophys. Geosystems 11, n/a-n/a. https://doi.org/10.1029/2009GC002694
994 Jackson, M.G., Hart, S.R., Saal, A.E., Shimizu, N., Kurz, M.D., Blusztajn, J.S., Skovgaard, A.C., 2008.
995 Globally elevated titanium, tantalum, and niobium (TITAN) in ocean island basalts with high
996 ^{34}$ He. Geochem. Geophys. Geosystems 9, n/a-n/a. https://doi.org/10.1029/2007GC001876
997 Jackson, M.G., Koga, K.T., Price, A., Konter, J.G., Koppers, A.A.P., Finlayson, V.A., Konrad, K., Hauri,
998 E.H., Kylander-Clark, A., Kelley, K.A., Kendrick, M.A., 2015. Deeply dredged submarine HIMU
999 glasses from the Tuvalu Islands, Polynesia: Implications for volatile budgets of recycled

oceanic crust. Geochem. Geophys. Geosystems 16, 3210–3234. https://doi.org/10.1002/2015GC005966

Jarosewich, E., Nelen, J.A., Norberg, J.A., 1980. Reference Samples for Electron Microprobe Analysis*. Geostand. Geoanalytical Res. 4, 43–47. https://doi.org/10.1111/j.1751-908X.1980.tb00273.x

Katz, R.F., Spiegelman, M., Langmuir, C.H., 2003. A new parameterization of hydrous mantle melting. Geochem. Geophys. Geosystems 4, n/a-n/a. https://doi.org/10.1029/2002GC000433

Kendrick, M.A., Hémond, C., Kamenetsky, V.S., Danyushevsky, L., Devey, C.W., Rodemann, T., Jackson, M.G., Perfit, M.R., 2017. Seawater cycled throughout Earth's mantle in partially serpentinized lithosphere. Nat. Geosci. 10, 222–228. https://doi.org/10.1038/ngeo2902

Kendrick, M.A., Jackson, M.G., Hauri, E.H., Phillips, D., 2015. The halogen (F, Cl, Br, I) and H2O systematics of Samoan lavas: Assimilated-seawater, EM2 and high-3He/4He components. Earth Planet. Sci. Lett. 410, 197–209. https://doi.org/10.1016/j.epsl.2014.11.026

Kendrick, M.A., Jackson, M.G., Kent, A.J.R., Hauri, E.H., Wallace, P.J., Woodhead, J., 2014. Contrasting behaviours of CO2, S, H2O and halogens (F, Cl, Br, and I) in enriched-mantle melts from Pitcairn and Society seamounts. Chem. Geol. 370, 69–81. https://doi.org/10.1016/j.chemgeo.2014.01.019

Koleszar, A.M., Saal, A.E., Hauri, E.H., Nagle, A.N., Liang, Y., Kurz, M.D., 2009. The volatile contents of the Galapagos plume; evidence for H2O and F open system behavior in melt inclusions. Earth Planet. Sci. Lett. 287, 442–452. https://doi.org/10.1016/j.epsl.2009.08.029

Kumamoto, K.M., Warren, J.M., Hauri, E.H., 2017. New SIMS reference materials for measuring water in upper mantle minerals. Am. Mineral. 102, 537–547. https://doi.org/10.2138/am-2017-5863CCBYNCND

Kurz, M.D., Curtice, J., Fornari, D., Geist, D., Moreira, M., 2009. Primitive neon from the center of the Galápagos hotspot. Earth Planet. Sci. Lett. 286, 23–34. https://doi.org/10.1016/j.epsl.2009.06.008

Kurz, M.D., Geist, D., 1999. Dynamics of the Galapagos hotspot from helium isotope geochemistry. Geochim. Cosmochim. Acta 63, 4139–4156. https://doi.org/10.1016/S0016-7037(99)00314-2

Lambart, S., Baker, M.B., Stolper, E.M., 2016. The role of pyroxenite in basalt genesis: Melt-PX, a melting parameterization for mantle pyroxenites between 0.9 and 5 GPa: Melt-PX: Pyroxenite Melting Model. J. Geophys. Res. Solid Earth 121, 5708–5735. https://doi.org/10.1002/2015JB012762

Lassiter, J.C., Hauri, E.H., Nikogosian, I.K., Barsczus, H.G., 2002. Chlorine–potassium variations in melt inclusions from Raivavae and Rapa, Austral Islands: constraints on chlorine recycling in the mantle and evidence for brine-induced melting of oceanic crust. Earth Planet. Sci. Lett. 202, 525–540. https://doi.org/10.1016/S0012-821X(02)00826-9

Le Roux, P., Shirey, S., Hauri, E., Perfit, M., Bender, J., 2006. The effects of variable sources, processes and contaminants on the composition of northern EPR MORB (8–10°N and 12–14°N): Evidence from volatiles (H2O, CO2, S) and halogens (F, Cl). Earth Planet. Sci. Lett. 251, 209–231. https://doi.org/10.1016/j.epsl.2006.09.012

Lissenberg, C.J., MacLeod, C.J., 2016. A Reactive Porous Flow Control on Mid-ocean Ridge Magmatic Evolution. J. Petrol. 57, 2195–2220. https://doi.org/10.1093/petrology/egw074

Lloyd, A.S., Ferriss, E., Ruprecht, P., Hauri, E.H., Jicha, B.R., Plank, T., 2016. An Assessment of Clinopyroxene as a Recorder of Magmatic Water and Magma Ascent Rate. J. Petrol. 57, 1865–1886. https://doi.org/10.1093/petrology/egw058

Lloyd, A.S., Ruprecht, P., Hauri, E.H., Rose, W., Gonnermann, H.M., Plank, T., 2014. NanoSIMS results from olivine-hosted melt embayments: Magma ascent rate during explosive basaltic eruptions. J. Volcanol. Geotherm. Res. 283, 1–18. https://doi.org/10.1016/j.jvolgeores.2014.06.002

1050 Lyons, J., Geist, D., Harpp, K., Diefenbach, B., Olin, P., Vervoort, J., 2007. Crustal growth by magmatic
1051 overplating in the Galápagos. Geology 35, 511. https://doi.org/10.1130/G23044A.1
1052 Maclennan, J., 2017. Bubble formation and decrepitation control the CO_2 content of olivine-hosted
1053 melt inclusions. Geochem. Geophys. Geosystems 18, 597–616.
1054 https://doi.org/10.1002/2016GC006633
1055 Maclennan, J., 2008. Concurrent Mixing and Cooling of Melts under Iceland. J. Petrol. 49, 1931–
1056 1953. https://doi.org/10.1093/petrology/egn052
1057 Marks, M.A.W., Kendrick, M.A., Eby, G.N., Zack, T., Wenzel, T., 2017. The F, Cl, Br and I Contents of
1058 Reference Glasses BHVO-2G, BIR-1G, BCR-2G, GSD-1G, GSE-1G, NIST SRM 610 and NIST SRM
1059 612. Geostand. Geoanalytical Res. 41, 107–122. https://doi.org/10.1111/ggr.12128
1060 Métrich, N., Zanon, V., Créon, L., Hildenbrand, A., Moreira, M., Marques, F.O., 2014. Is the 'Azores
1061 Hotspot' a Wetspot? Insights from the Geochemistry of Fluid and Melt Inclusions in Olivine
1062 of Pico Basalts. J. Petrol. 55, 377–393. https://doi.org/10.1093/petrology/egt071
1063 Michael, P., 1995. Regionally distinctive sources of depleted MORB: Evidence from trace elements
1064 and H2O. Earth Planet. Sci. Lett. 131, 301–320. https://doi.org/10.1016/0012-
1065 821X(95)00023-6
1066 Michael, P.J., Cornell, W.C., 1998. Influence of spreading rate and magma supply on crystallization
1067 and assimilation beneath mid-ocean ridges: Evidence from chlorine and major element
1068 chemistry of mid-ocean ridge basalts. J. Geophys. Res. Solid Earth 103, 18325–18356.
1069 https://doi.org/10.1029/98JB00791
1070 Miller, W.G.R., Maclennan, J., Shorttle, O., Gaetani, G.A., Le Roux, V., Klein, F., 2019. Estimating the
1071 carbon content of the deep mantle with Icelandic melt inclusions. Earth Planet. Sci. Lett. 523,
1072 115699. https://doi.org/10.1016/j.epsl.2019.07.002
1073 Nazzareni, S., Barbarossa, V., Skogby, H., Zanon, V., Petrelli, M., 2020. Magma water content of Pico
1074 Volcano (Azores Islands, Portugal): a clinopyroxene perspective. Contrib. Mineral. Petrol.
1075 175, 87. https://doi.org/10.1007/s00410-020-01728-7
1076 Novella, D., Frost, D.J., Hauri, E.H., Bureau, H., Raepsaet, C., Roberge, M., 2014. The distribution of
1077 H2O between silicate melt and nominally anhydrous peridotite and the onset of hydrous
1078 melting in the deep upper mantle. Earth Planet. Sci. Lett. 400, 1–13.
1079 https://doi.org/10.1016/j.epsl.2014.05.006
1080 O'Leary, J.A., Gaetani, G.A., Hauri, E.H., 2010. The effect of tetrahedral Al3+ on the partitioning of
1081 water between clinopyroxene and silicate melt. Earth Planet. Sci. Lett. 297, 111–120.
1082 https://doi.org/10.1016/j.epsl.2010.06.011
1083 Peterson, M.E., Saal, A.E., Kurz, M.D., Hauri, E.H., Blusztajn, J.S., Harpp, K.S., Werner, R., Geist, D.J.,
1084 2017. Submarine Basaltic Glasses from the Galapagos Archipelago: Determining the Volatile
1085 Budget of the Mantle Plume. J. Petrol. 58, 1419–1450.
1086 https://doi.org/10.1093/petrology/egx059
1087 Poland, M.P., 2014. Contrasting Volcanism in Hawai'i and the Galápagos, in: Harpp, K.S.,
1088 Mittelstaedt, E., d'Ozouville, N., Graham, D.W. (Eds.), Geophysical Monograph Series. John
1089 Wiley & Sons, Inc, Hoboken, New Jersey, pp. 5–26.
1090 https://doi.org/10.1002/9781118852538.ch2
1091 Roeder, P.L., Emslie, R.F., 1970. Olivine-liquid equilibrium. Contr Miner. Pet. 29, 275–289.
1092 https://doi.org/10.1007/BF00371276
1093 Rosenthal, A., Yaxley, G.M., Green, D.H., Hermann, J., Kovács, I., Spandler, C., 2015. Continuous
1094 eclogite melting and variable refertilisation in upwelling heterogeneous mantle. Sci. Rep. 4.
1095 https://doi.org/10.1038/srep06099
1096 Rudge, J.F., Maclennan, J., Stracke, A., 2013. The geochemical consequences of mixing melts from a
1097 heterogeneous mantle. Geochim. Cosmochim. Acta 114, 112–143.
1098 https://doi.org/10.1016/j.gca.2013.03.042

1099 Saal, A., Kurz, M., Hart, S., Blusztajn, J., Blicherttoft, J., Liang, Y., Geist, D., 2007. The role of
1100 lithospheric gabbros on the composition of Galapagos lavas. Earth Planet. Sci. Lett. 257,
1101 391–406. https://doi.org/10.1016/j.epsl.2007.02.040
1102 Saal, A.E., Hauri, E.H., Langmuir, C.H., Perfit, M.R., 2002. Vapour undersaturation in primitive mid-
1103 ocean-ridge basalt and the volatile content of Earth's upper mantle. Nature 419, 451–455.
1104 https://doi.org/10.1038/nature01073
1105 Sheather, S.J., Jones, M.C., 1991. A Reliable Data-Based Bandwidth Selection Method for Kernel
1106 Density Estimation. J. R. Stat. Soc. Ser. B Methodol. 53, 683–690.
1107 https://doi.org/10.1111/j.2517-6161.1991.tb01857.x
1108 Shimizu, K., Saal, A.E., Myers, C.E., Nagle, A.N., Hauri, E.H., Forsyth, D.W., Kamenetsky, V.S., Niu, Y.,
1109 2016. Two-component mantle melting-mixing model for the generation of mid-ocean ridge
1110 basalts: Implications for the volatile content of the Pacific upper mantle. Geochim.
1111 Cosmochim. Acta 176, 44–80. https://doi.org/10.1016/j.gca.2015.10.033
1112 Shishkina, T.A., Botcharnikov, R.E., Holtz, F., Almeev, R.R., Jazwa, A.M., Jakubiak, A.A., 2014.
1113 Compositional and pressure effects on the solubility of H2O and CO2 in mafic melts. Chem.
1114 Geol. 388, 112–129. https://doi.org/10.1016/j.chemgeo.2014.09.001
1115 Shishkina, T.A., Botcharnikov, R.E., Holtz, F., Almeev, R.R., Portnyagin, M.V., 2010. Solubility of H2O-
1116 and CO2-bearing fluids in tholeiitic basalts at pressures up to 500MPa. Chem. Geol. 277,
1117 115–125. https://doi.org/10.1016/j.chemgeo.2010.07.014
1118 Sides, I.R., Edmonds, M., Maclennan, J., Swanson, D.A., Houghton, B.F., 2014. Eruption style at
1119 Kīlauea Volcano in Hawai'i linked to primary melt composition. Nat. Geosci. 7, 464–469.
1120 https://doi.org/10.1038/ngeo2140
1121 Steele-Macinnis, M., Esposito, R., Bodnar, R.J., 2011. Thermodynamic Model for the Effect of Post-
1122 entrapment Crystallization on the H2O-CO2 Systematics of Vapor-saturated, Silicate Melt
1123 Inclusions. J. Petrol. 52, 2461–2482. https://doi.org/10.1093/petrology/egr052
1124 Stock, M.J., Bagnardi, M., Neave, D.A., Maclennan, J., Bernard, B., Buisman, I., Gleeson, M.L.M.,
1125 Geist, D., 2018. Integrated Petrological and Geophysical Constraints on Magma System
1126 Architecture in the Western Galápagos Archipelago: Insights From Wolf Volcano. Geochem.
1127 Geophys. Geosystems 19, 4722–4743. https://doi.org/10.1029/2018GC007936
1128 Stock, M.J., Geist, D., Neave, D.A., Gleeson, M.L.M., Bernard, B., Howard, K.A., Buisman, I.,
1129 Maclennan, J., 2020. Cryptic evolved melts beneath monotonous basaltic shield volcanoes in
1130 the Galápagos Archipelago. Nat. Commun. 11, 3767. https://doi.org/10.1038/s41467-020-
1131 17590-x
1132 Stock, M.J., Humphreys, M.C.S., Smith, V.C., Isaia, R., Pyle, D.M., 2016. Late-stage volatile saturation
1133 as a potential trigger for explosive volcanic eruptions. Nat. Geosci. 9, 249–254.
1134 https://doi.org/10.1038/ngeo2639
1135 Sun, S. -s., McDonough, W.F., 1989. Chemical and isotopic systematics of oceanic basalts:
1136 implications for mantle composition and processes. Geol. Soc. Lond. Spec. Publ. 42, 313–
1137 345. https://doi.org/10.1144/GSL.SP.1989.042.01.19
1138 Turner, M., Turner, S., Mironov, N., Portnyagin, M., Hoernle, K., 2017. Can magmatic water contents
1139 be estimated from clinopyroxene phenocrysts in some lavas? A case study with implications
1140 for the origin of the Azores Islands. Chem. Geol. 466, 436–445.
1141 https://doi.org/10.1016/j.chemgeo.2017.06.032
1142 Ubide, T., Galé, C., Larrea, P., Arranz, E., Lago, M., 2014. Antecrysts and their effect on rock
1143 compositions: The Cretaceous lamprophyre suite in the Catalonian Coastal Ranges (NE
1144 Spain) 20.
1145 Vasconez, F., Ramón, P., Hernandez, S., Hidalgo, S., Bernard, B., Ruiz, M., Alvarado, A., La Femina, P.,
1146 Ruiz, G., 2018. he different characteristics of the recent eruptions of Fernandina and Sierra
1147 Negra volcanoes (Galápagos, Ecuador). Volcanica 1, 127–133.
1148 https://doi.org/10.30909/vol.01.02.127133

Vidito, C., Herzberg, C., Gazel, E., Geist, D., Harpp, K., 2013. Lithological structure of the Galápagos Plume: Lithological Structure Galpagos Plume. Geochem. Geophys. Geosystems 14, 4214–4240. https://doi.org/10.1002/ggge.20270

Villagómez, D.R., Toomey, D.R., Geist, D.J., Hooft, E.E.E., Solomon, S.C., 2014. Mantle flow and multistage melting beneath the Galápagos hotspot revealed by seismic imaging. Nat. Geosci. 7, 151–156. https://doi.org/10.1038/ngeo2062

Wade, J.A., Plank, T., Hauri, E.H., Kelley, K.A., Roggensack, K., Zimmer, M., 2008. Prediction of magmatic water contents via measurement of H2O in clinopyroxene phenocrysts. Geology 36, 799. https://doi.org/10.1130/G24964A.1

Weiss, Y., Class, C., Goldstein, S.L., Hanyu, T., 2016. Key new pieces of the HIMU puzzle from olivines and diamond inclusions. Nature 537, 666–670. https://doi.org/10.1038/nature19113

White, W.M., 2010. Oceanic Island Basalts and Mantle Plumes: The Geochemical Perspective. Annu. Rev. Earth Planet. Sci. 38, 133–160. https://doi.org/10.1146/annurev-earth-040809-152450

White, W.M., McBirney, A.R., Duncan, R.A., 1993. Petrology and geochemistry of the Galápagos Islands: Portrait of a pathological mantle plume. J. Geophys. Res. Solid Earth 98, 19533–19563. https://doi.org/10.1029/93JB02018

Wieser, P., Iacovino, K., Matthews, S., Moore, G., Allison, C., 2021. VESIcal Part II: A critical approach to volatile solubility modelling using an open-source Python3 engine (preprint). Earth Sciences. https://doi.org/10.31223/X5K03T

Wieser, P.E., Edmonds, M., Maclennan, J., Jenner, F.E., Kunz, B.E., 2019. Crystal scavenging from mush piles recorded by melt inclusions. Nat. Commun. 10, 5797. https://doi.org/10.1038/s41467-019-13518-2

Wieser, P.E., Lamadrid, H., Maclennan, J., Edmonds, M., Matthews, S., Iacovino, K., Jenner, F.E., Gansecki, C., Trusdell, F., Lee, R.L., Ilyinskaya, E., 2020. Reconstructing Magma Storage Depths for the 2018 Kīlauean Eruption from Melt inclusion CO2 Contents: The Importance of Vapor Bubbles. Geochem. Geophys. Geosystems. https://doi.org/10.1029/2020GC009364

Witham, F., Blundy, J., Kohn, S.C., Lesne, P., Dixon, J., Churakov, S.V., Botcharnikov, R., 2012. SolEx: A model for mixed COHSCl-volatile solubilities and exsolved gas compositions in basalt. Comput. Geosci. 45, 87–97. https://doi.org/10.1016/j.cageo.2011.09.021

Wood, B.J., Blundy, J.D., 1997. A predictive model for rare earth element partitioning between clinopyroxene and anhydrous silicate melt. Contrib. Mineral. Petrol. 129, 166–181. https://doi.org/10.1007/s004100050330

Workman, R.K., Hauri, E., Hart, S.R., Wang, J., Blusztajn, J., 2006. Volatile and trace elements in basaltic glasses from Samoa: Implications for water distribution in the mantle. Earth Planet. Sci. Lett. 241, 932–951. https://doi.org/10.1016/j.epsl.2005.10.028

Zhang, Y., Ni, H., 2010. Diffusion of H, C, and O Components in Silicate Melts. Rev. Mineral. Geochem. 72, 171–225. https://doi.org/10.2138/rmg.2010.72.5

Zhang, Y., Ni, H., Chen, Y., 2010. Diffusion Data in Silicate Melts. Rev. Mineral. Geochem. 72, 311–408. https://doi.org/10.2138/rmg.2010.72.8

Zindler, A., Hart, S., 1986. Helium: problematic primordial signals. Earth Planet. Sci. Lett. 79, 1–8. https://doi.org/10.1016/0012-821X(86)90034-8

FIGURE CAPTIONS

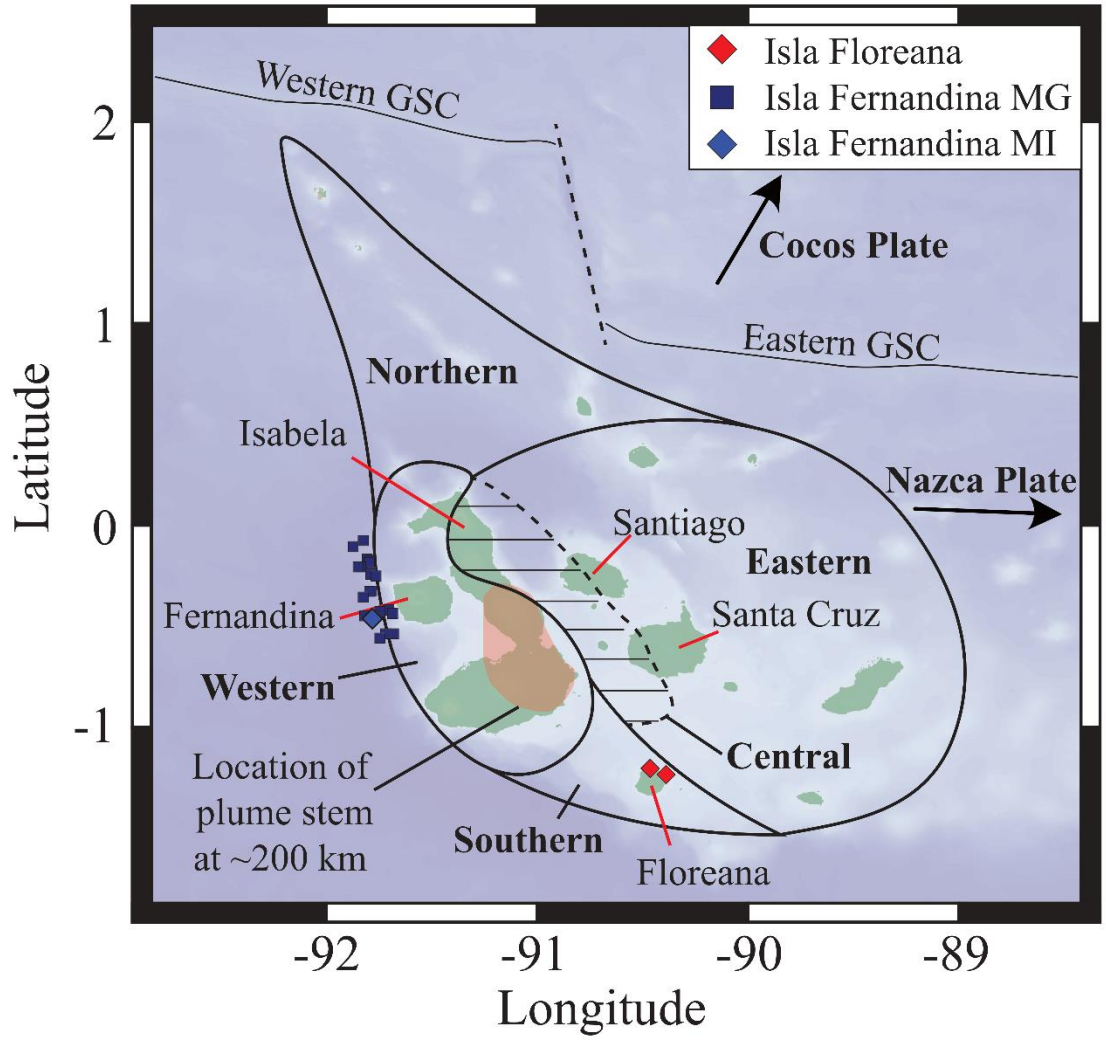

Figure 1 – Map of the Galápagos Archipelago. The approximate location of the various isotopic components expressed in the composition of the Galápagos basalts are taken from Hoernle et al. (2000) and Gleeson et al. (2020b). The location of the mantle plume at ~200 km depth (from Villagómez et al., 2014) together with the location of samples used in this study (from Koleszar et al. (2009), Peterson et al. (2017) and Gleeson et al. (2020a)) are also shown.

This manuscript represents a pre-print of a manuscript that has undergone peer-review and has been accepted for publication with Geochimica et Cosmochimica Acta.

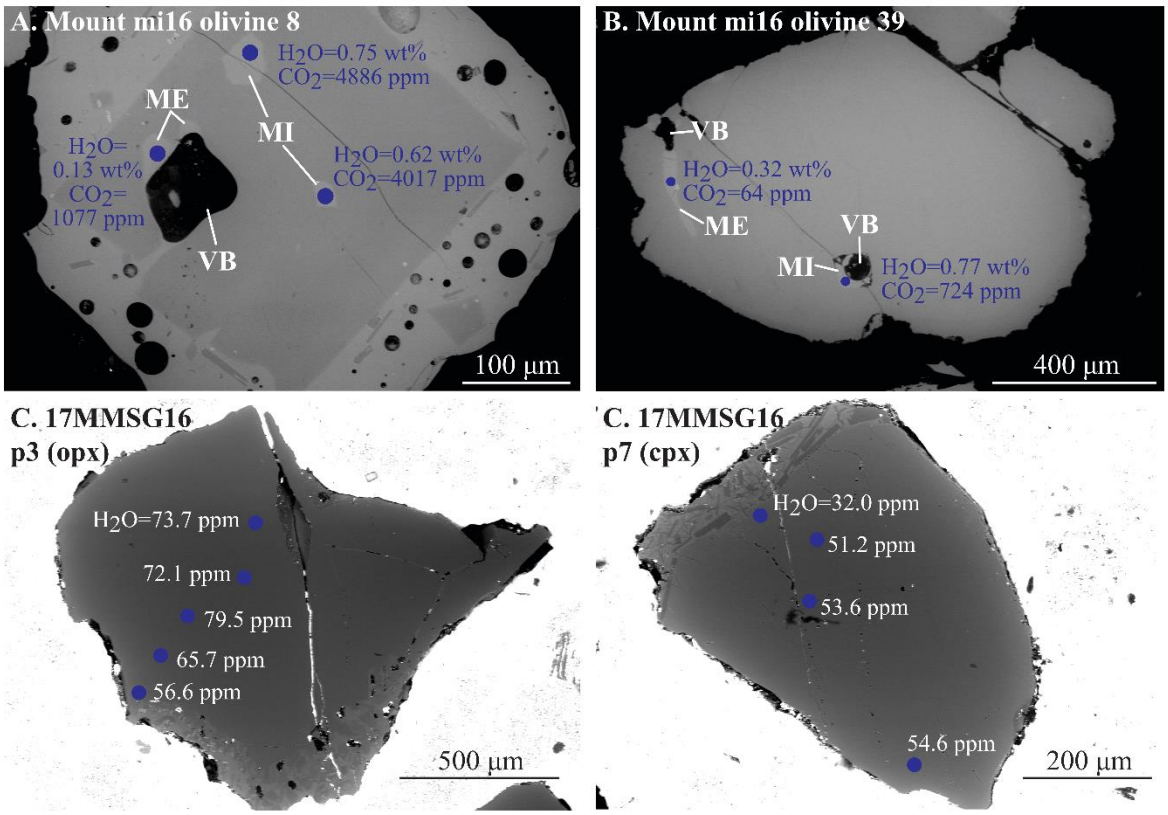

Figure 2 – SEM images of olivine-hosted melt inclusions and orthopyroxene and clinopyroxene grains mounted in indium. **A.** Small olivine crystal (~400 µm across) with 2 melt inclusions that both preserve relatively high CO_2 contents. A small embayment on the edge of this crystal has low H_2O contents consistent with degassing and diffusive loss of H_2O from this melt. **B.** A melt inclusion with a large, possibly co-entrapped, vapour bubble in a larger olivine crystal. Also present in this crystal is a relatively long (~200 µm) melt embayment that preserves high melt H_2O contents (~0.33 wt%). **C.** H_2O content of an orthopyroxene crystal from scoria sample 17MMSG16. The H_2O content in the core of this crystal is relatively constant, but the rim analysis returns notably lower H_2O contents than the core analyses. **D.** A similar spatial relationship is seen in some of the clinopyroxene crystals from Floreana, where the rim analysis returns slightly lower H_2O contents than the core analyses. MI – melt inclusion; ME – melt embayment; VB – vapour bubble.

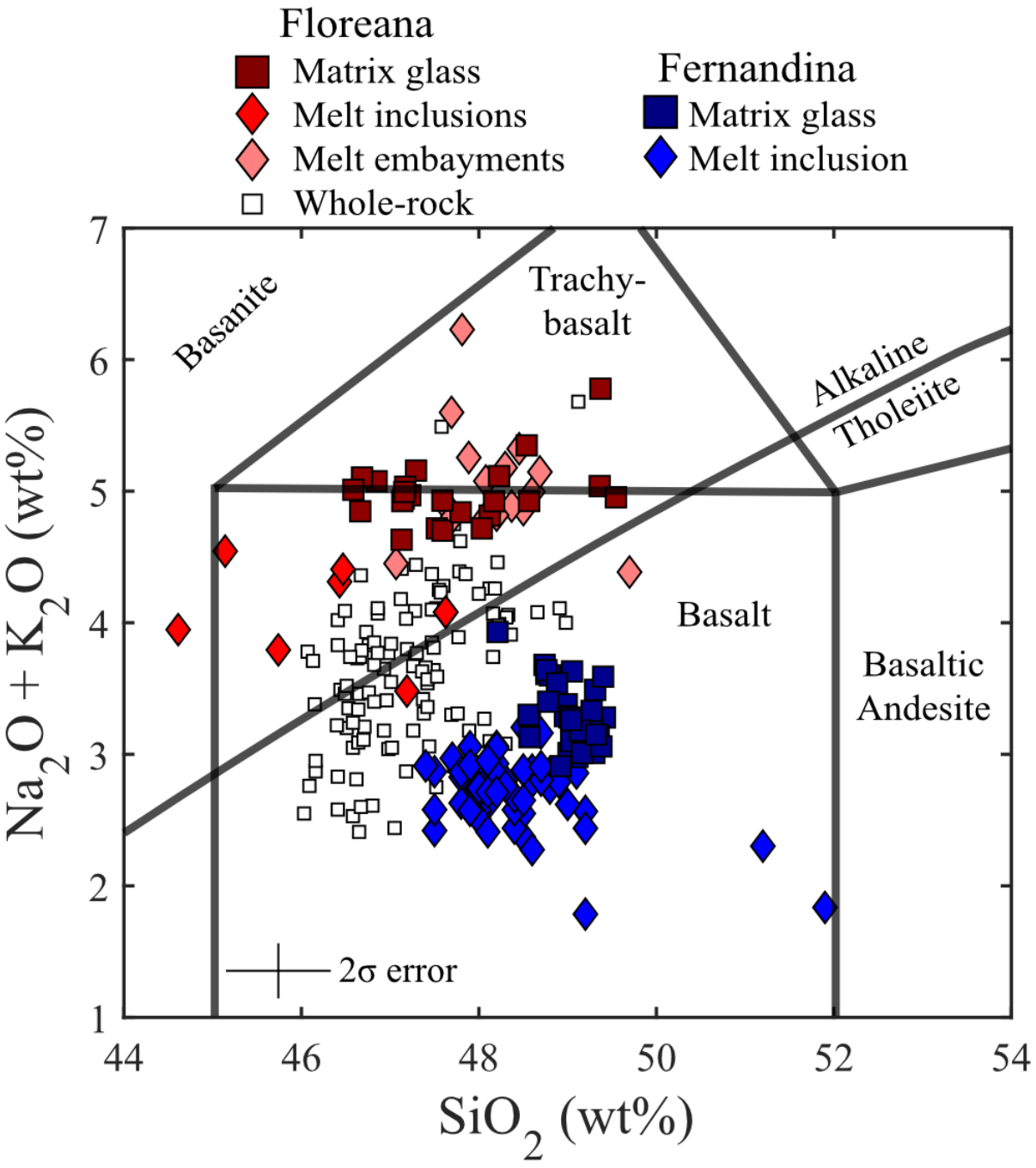

Figure 3 – Total alkalis versus silica plot of the Floreana melt inclusions, melt embayments and matrix glasses (Irvine and Baragar, 1971). The $Na_2O + K_2O$ content of most Floreana matrix glasses, and the majority of melt inclusions and melt embayments straddle the divide between basalts and trachy-basalts. Floreana matrix glass data is taken from Gleeson et al. (2020a) and the whole-rock data is taken from Harpp et al. (2014). Data from Isla Fernandina is taken from Koleszar et al. (2009) and Peterson et al. (2017).

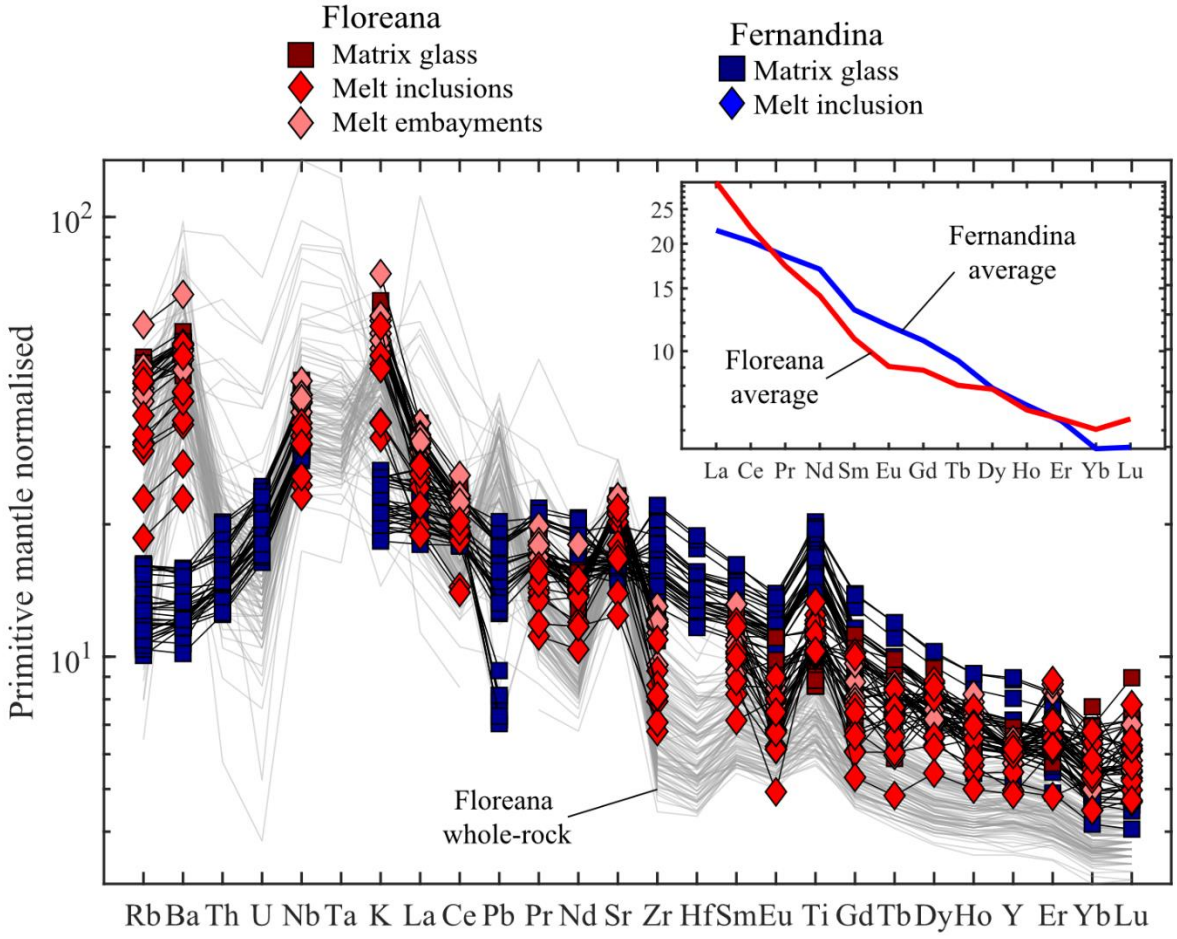

Figure 4 – Trace element composition of the Fernandina and Floreana basalts. The Floreana basalts contain high concentrations of fluid-mobile trace elements (such as Ba; Harpp et al., 2014). This signature is observed in both our new melt inclusion and matrix glass data as well as published whole-rock data (Harpp et al., 2014). The Floreana basalts display concave-up rare earth element (REE) signatures, with steep light-to-middle REE slopes and shallow middle-to-heavy REE slopes (inset). Data from Isla Fernandina is from Koleszar et al. (2009) and Peterson et al. (2017). Primitive mantle values are taken from Sun and McDonough (1989).

This manuscript represents a pre-print of a manuscript that has undergone peer-review and has been accepted for publication with Geochimica et Cosmochimica Acta.

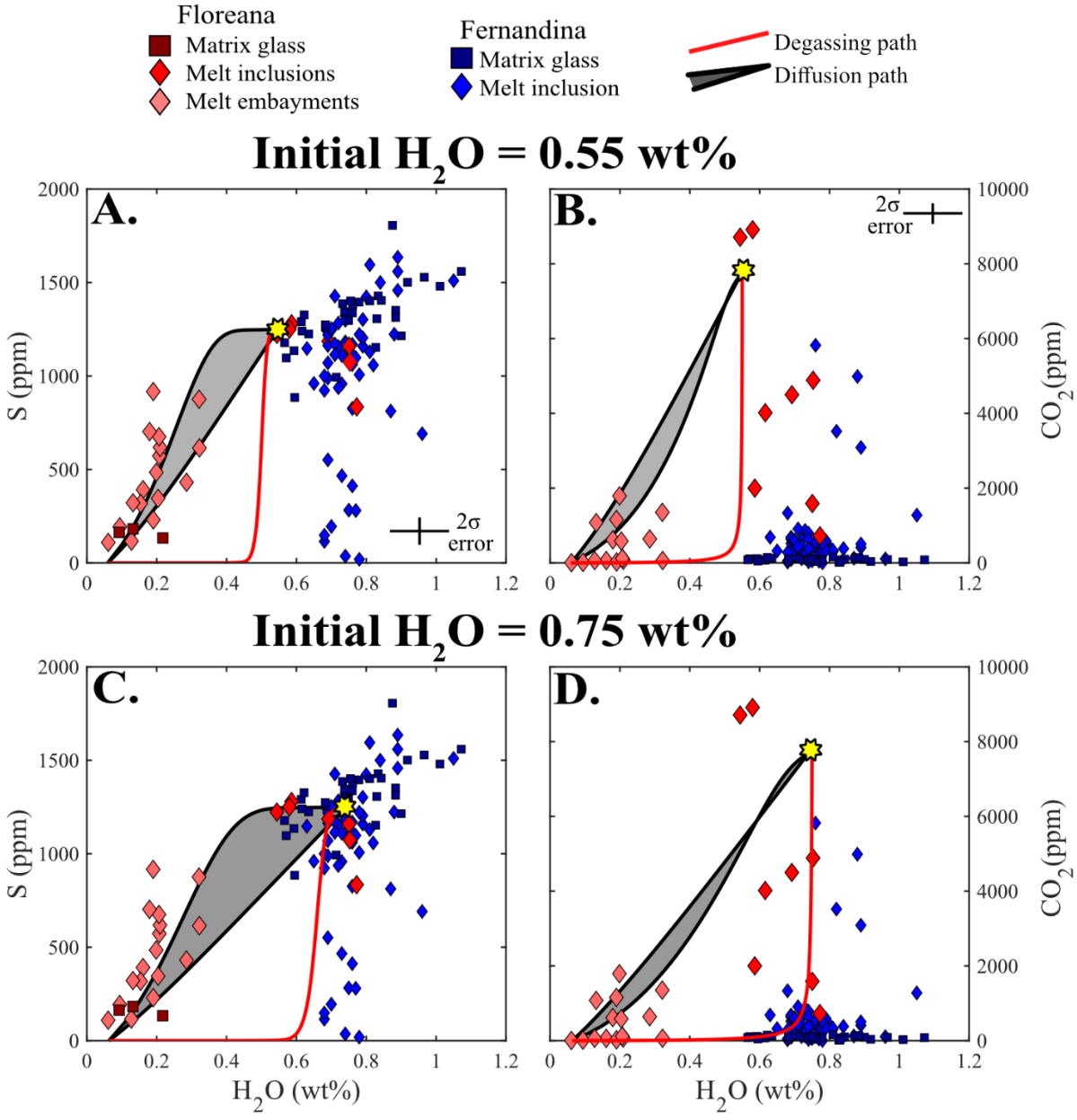

Figure 5 – Volatile systematics of the Floreana melt inclusions and melt embayments. Grey shaded areas in all plots reveal the range of compositions that are observed in modelled embayments following combined decompression – diffusion models. Results are shown for all models that initiate at 750 MPa with decompression rates between 0.005 and 0.5 MPa/s. The H_2O vs S systematics of the Floreana melt embayments can be matched by models that have initial melt embayment H_2O contents between 0.55 wt% (**A., B.**) and 0.75 wt% (**C., D**). Fernandina data from Koleszar et al. (2009) and Peterson et al. (2017).

Figure 6 – Correlation matrix calculated from the trace and volatile element concentrations of the Floreana melt inclusions and melt embayments. The colour of each square is controlled by the correlation coefficient of the two elements of interest (red = positive correlation; blue = negative correlation). The correlation coefficient of each square is shown, white lettering indicates that the correlation is significant at the 95% confidence interval..

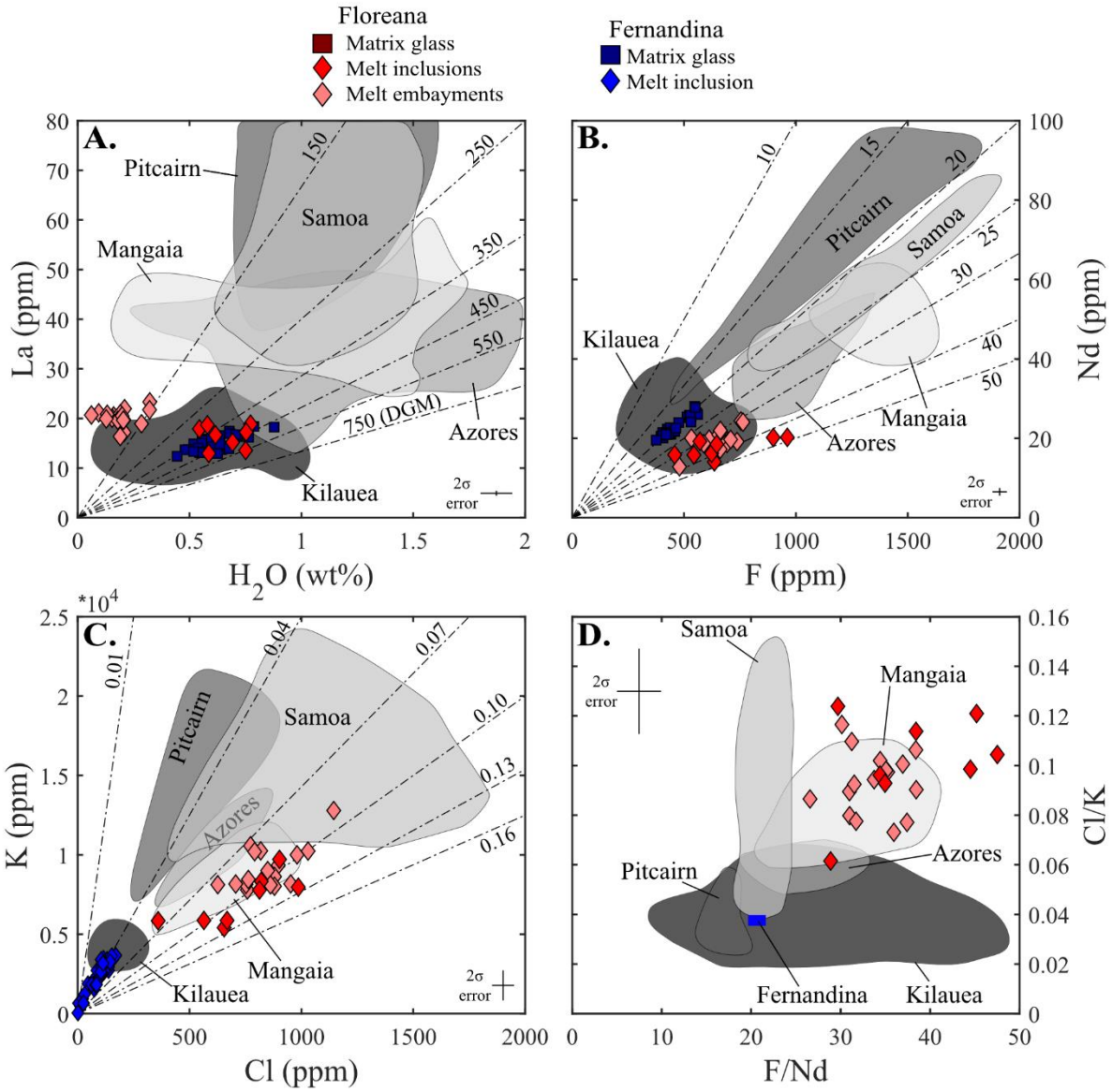

Figure 7 – Volatile vs non-volatile trace element systematics of the Floreana and Fernandina basalts. Lines of constant volatile to non-volatile trace element ratios (i.e. constant H_2O/La, F/Nd, or Cl/K) are displayed in panels **A.** to **C.**. **A**. There is a large range in the H_2O contents of the Floreana melt inclusions and melt embayments, but only a narrow range of La contents. DGM refers to the Depleted Galápagos Mantle and the H_2O/La ratio of this component is constrained in Gleeson and Gibson (2021). **B.** F vs Nd, the F content of the Floreana basalts are regularly higher than the F contents of basalts from Fernandina at an equivalent Nd concentration (data from Peterson et al., 2017). **C.** Cl vs K, the Floreana basalts have consistently higher Cl and K contents than melt inclusions from Fernandina (Koleszar et al., 2009). **D.** The high F/Nd and Cl/K ratios of the Floreana melt inclusions and melt embayments is rarely observed in ocean island basalts. Data presented in this figure from Cabral et al. (2014); Kendrick et al. (2014); Koleszar et al. (2009); Métrich et al. (2014); Peterson et al. (2017); Sides et al. (2014); Workman et al. (2006) and this study.

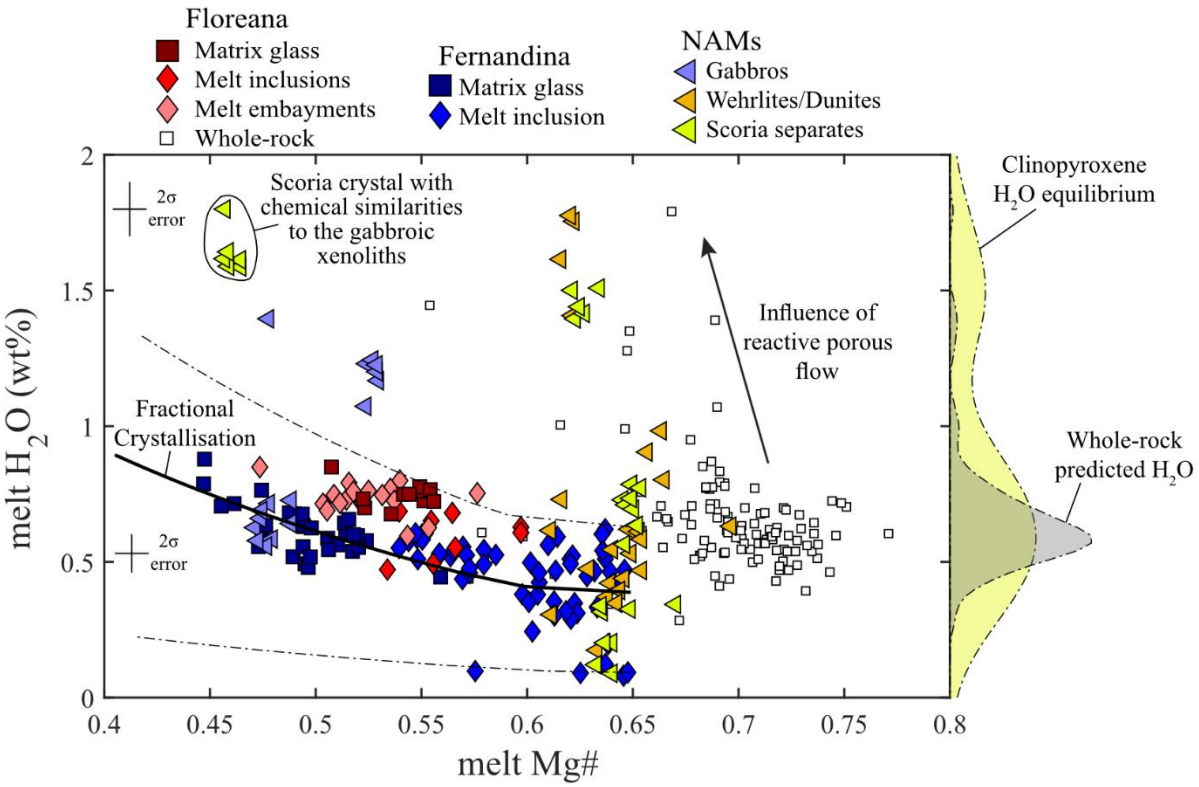

Figure 8 – Summary of the content and evolution of volatiles in magmas from Floreana and Fernandina. Glass compositions, excluding the submarine glass analyses from Fernandina, and whole-rock compositions represent predicted H_2O concentrations that are calculated using the La content measured in each sample and the H_2O/La ratio that characterises the Fernandina and Floreana magmas. The values shown for the submarine glasses from Fernandina are the brine-corrected H_2O contents. Density distributions on the right-hand axis show the distribution of predicted H_2O concentrations for the Floreana whole-rocks (grey; Harpp et al., 2014) and for core pyroxene analyses (yellow; excluding crystals that show a chemical affinity to the gabbroic xenoliths). Black lines represent crystallisation models carried out in Petrolog v3.1.1.3 (Danyushevsky and Plechov, 2011) to simulate how H_2O would change during crystallisation of: (i) the most enriched; (ii) the average; and (iii) the most depleted compositions measured in the Fernandina melt inclusions (Peterson et al., 2017). Crystallisation models are carried out at ~300 MPa and QFM, appropriate for western Galápagos volcanic systems (Stock et al., 2018). 2σ errors represent the fully propagated analytical precision for both H_2O-rich and H_2O-poor clinopyroxenes. Equilibrium melt Mg# is calculated for the clinopyroxenes using the formulation of Wood and Blundy (1997) assuming that the Fe^{3+}/Fe_{tot} ratio of the melt is ~0.15. Kernel density distribution bandwidths are calculated using the method of Sheather and Jones (1991).

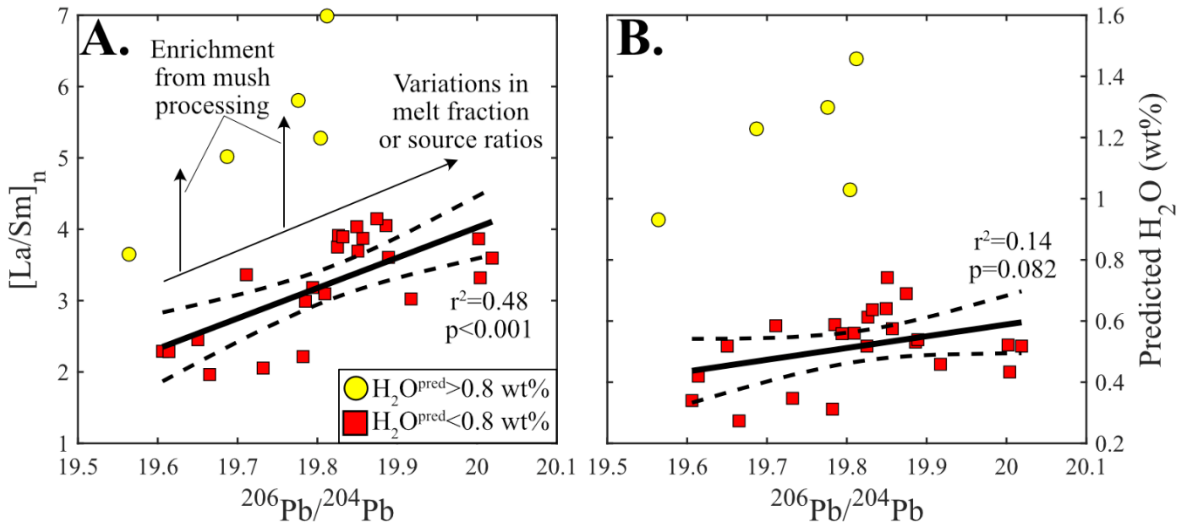

1270

1271 **Figure 9 –** Pb isotope vs trace element systematics of the Floreana whole-rock (data from Harpp et
1272 al. 2014). In basalts with predicted H_2O contents <0.8 wt%, there is a statistically significant
1273 correlation (at the 99% confidence level) between the isotopic and trace element systematics of the
1274 Floreana basalts. However, those basalts with predicted H_2O contents >0.8 wt% do not follow this
1275 correlation and are isotopically indistinguishable from the rest of the Floreana basalts. Data from
1276 Harpp et al. (2014)

This manuscript represents a pre-print of a manuscript that has undergone peer-review and has been accepted for publication with Geochimica et Cosmochimica Acta.

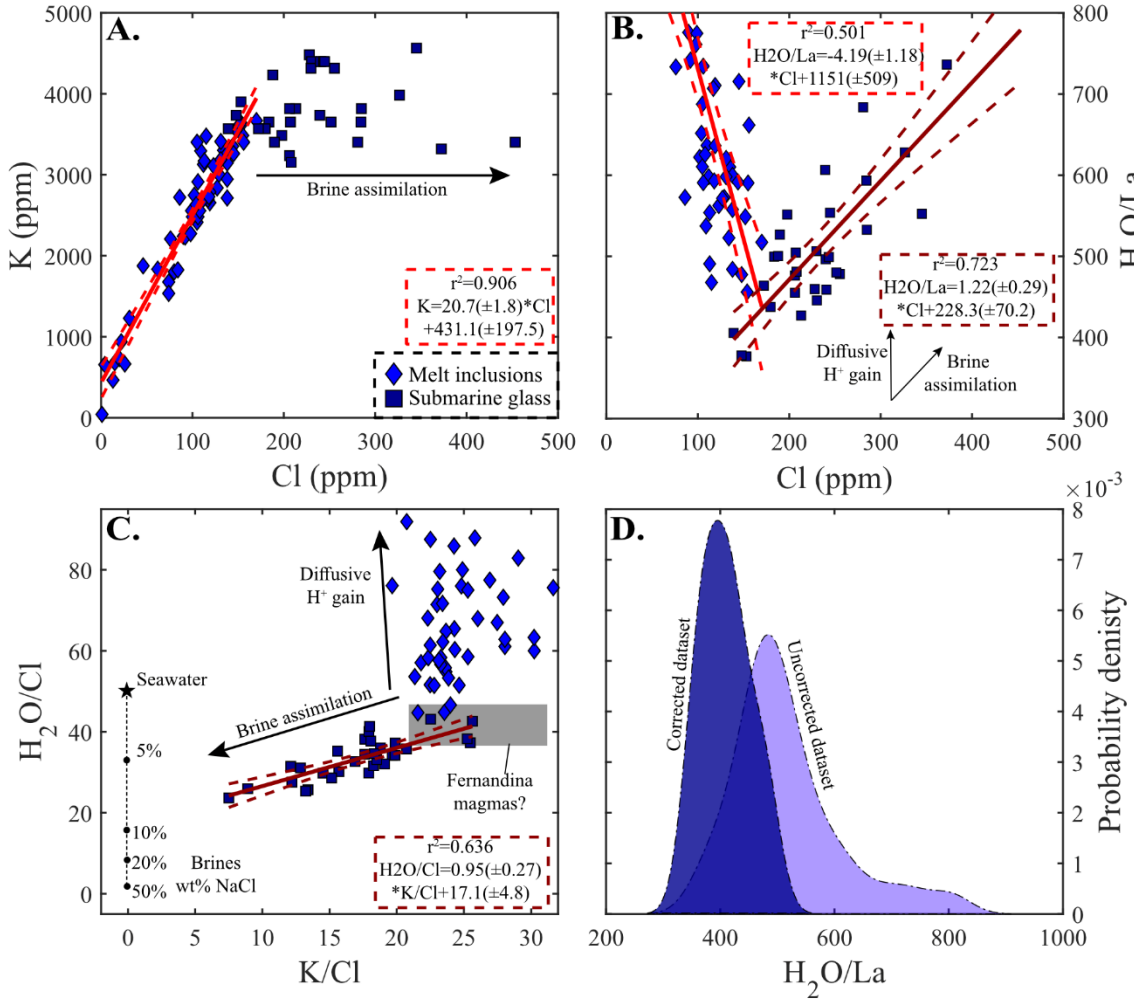

Figure 10 – Insights into the volatile content of the Isla Fernandina basalts. **A.** There is a statistically significant correlation between K and Cl in the melt inclusion dataset of Koleszar et al. (2009), but the Cl concentrations measured in submarine glasses from Fernandina extend to much higher values at approximately constant K concentrations (Peterson et al., 2017). **B.** Diverging trends of Cl vs H_2O/La are hypothesised to result from assimilation of a Cl-rich hydrothermal brine prior to eruption of the Fernandina basalts, and diffusive migration of H^+ between olivine-hosted melt inclusions and the carrier melt (incompatible trace element depleted melt inclusions from Koleszar et al. (2009) are excluded from the shown correlation). **C.** Evidence for assimilation of hydrothermal brines comes from the correlation between K/Cl and H_2O/Cl. The intersection of this linear regression with the y-axis gives an estimate of the H_2O/Cl content of the assimilated component. The grey regions in panels **B.** and **C.** display the hypothesised composition of primary Fernandina magmas. Estimated composition of the initial Fernandina magmas are shown in grey. **D.** Probability density distribution for H_2O/La in the uncorrected (light blue) and brine-assimilation corrected (dark blue) submarine glass dataset. Dashed lines in **A., B., and C.** represent the 95% confidence limits on the various regression lines.

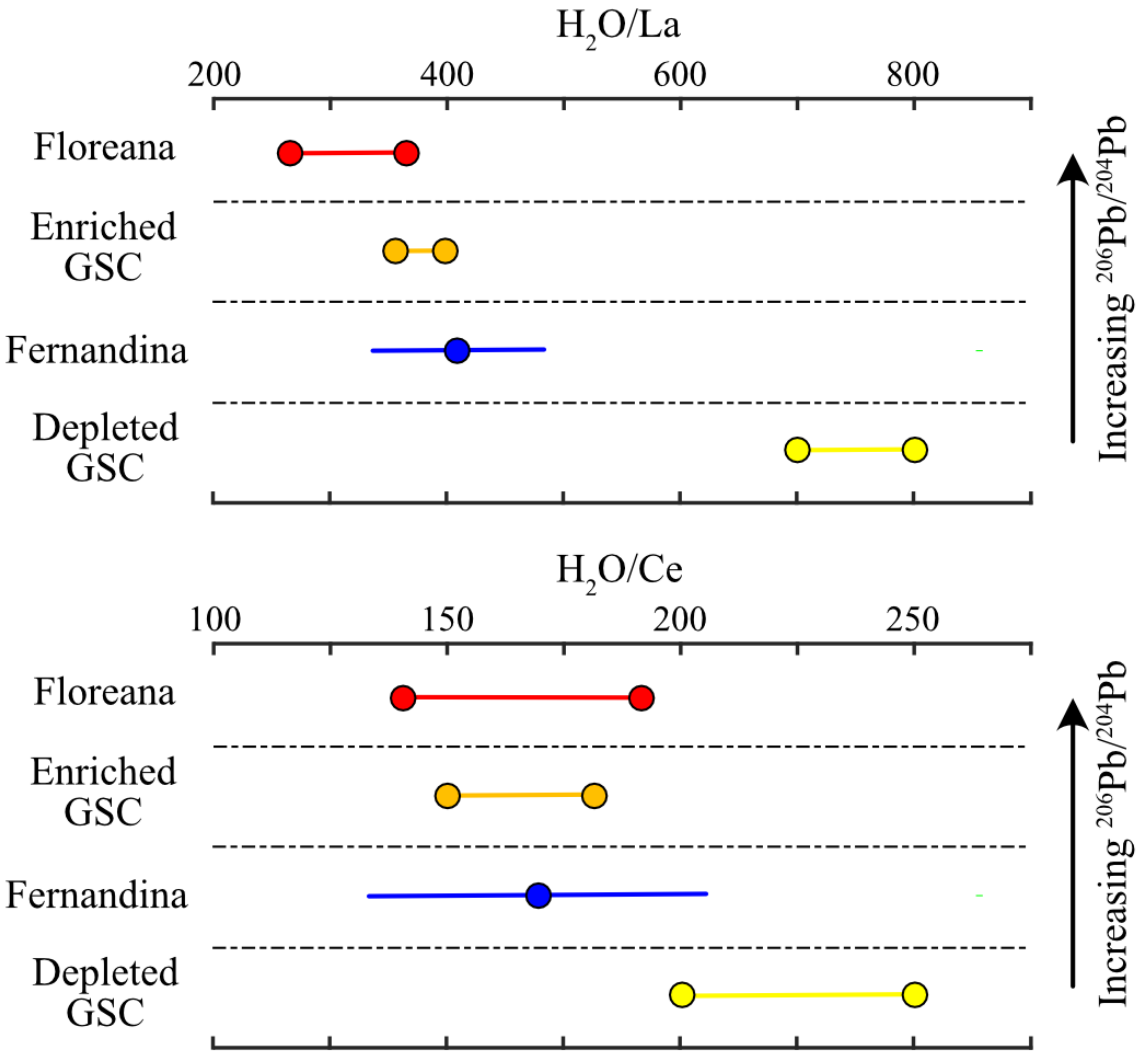

Figure 11 – Summary of the H_2O/REE systematics of basalts from different regions of the Galápagos Archipelago. The H_2O/La ratios that characterise depleted and enriched basalts from the GSC are taken from Gleeson and Gibson (2021). In most cases the range of predicted H_2O/La and H_2O/Ce ratios are shown, with the circular symbols representing the maximum and minimum estimate. For Fernandina, however, the circle represents the mean of the brine-corrected H_2O/La and H_2O/Ce ratios in the Fernandina submarine basalts, with the solid line representing the 2σ deviation around this mean.